Shunted optimal vibration energy harvesting control of discontinuous smart beams

M.F. Lumentut[a], **Y.C. Shu**[b]

[a] School of Civil and Mechanical Engineering, Curtin University, Perth, Australia

[b] Institute of Applied Mechanics, National Taiwan University, Taiwan, ROC

Emails: m.lumentut@curtin.edu.au and yichung@iam.ntu.edu.tw

Abstract

This paper presents an adaptive dynamic analysis of discontinuous smart beam energy harvester systems using a shunt vibration control. The smart structural systems, connected with the shunt and harvesting circuit interfaces, consist of the three types of non-homogeneous structural combinations with different piezoelectric materials. The constitutive coupled dynamic equations with full variational parameters are reduced using the charge type-based Hamiltonian mechanics and the Ritz method-based weak-form analytical approach. Unlike the conventional techniques, this study elaborates the appearance of the two resonances with a wider shift on a specific range of the optimal power output frequencies, using only the first mode of the smart structural systems. Moreover, the two-equal peak of the optimal response may potentially occur to appear not only at the first resonance, but also at the second resonance. This intrinsically represents strong electromechanical effect, depending on the properties and thicknesses of piezoelectric materials and the circuit parameters. The accuracy of the theoretical method is tested using the iterative computational process of the optimal frequency response with full coupled electromechanical system parameters. Further details of the parametric studies are discussed to show the prediction of the energy harvesting with the ability of tuning an adaptive frequency response.

Keywords: Adaptive response; Laminated smart structures; Control system; Vibration energy harvesting; Piezoelectricity.

1 Introduction

Smart structure with the piezoelectric material has become an attractive research area that provides capabilities to generate the electric charge and produce the motion. In specification of smart structure applications, the control system becomes one of today's profound research trends with the key components of piezoelectric element and non-active structure. Moreover, the configuration of the system itself obviously underlies on the varieties of the physical and technical studies as proposed by many researchers. The investigation of the system with either smart beam or plate structure covers wide ranging control strategies such as the structural control [1-7], shape control [8-11], feedback gain control [12-14], and shunt control [15-17]. In particular attentions to the vibration suppression using the shunt control, the resonance of the smart structure with the selected mode can be tuned into the desired frequency resulting in the reduction of the amplitude [18-19]. Earlier studies have investigated a tuning resonance of the smart structure using the LC circuit-shunted piezo-system [20] and the RL-shunted piezo-system [21–24]. For stabilising the signal of the shunt circuit parameters, the synchronized switching technique was also developed to improve the performance of the vibration reduction [25,26]. Furthermore, various vibration suppression methods for several modes of the

structural system have been developed using the multiple circuit branches with the RLC-shunted piezo-systems [15,17,27-29]. Since the required inductance value in the shunt circuit is very high, the synthetic inductor or gyrator [30]-[33] was developed in order to tune the desired frequency.

Another recent application of the smart structure for converting the electrical energy from the surrounding vibration environment has been developed using various physical systems and theoretical methods. The key strategy of the piezoelectric structure power harvesters can be found in the use of a tip mass and a shunt impedance circuit for the frequency tuning system. Unlike the control system-based smart structure for vibration suppression, the energy harvesting system requires the optimal physical structure with a relatively small scale, allowing to produce the essential frequency shift from high to low value and maximise the power output. The reason is that it is designed to be attached on the main structures (e.g. civil engineering structure, automobile, lightweight aerospace, and even biomechanical system of human body) that normally excite the vibration. This unused mechanical motion can be benefit for the energy conversion so as to recharge battery and enable to powering wireless sensor device for the structural health monitoring. In this scenario, most notably structure model has included the cantilever laminated piezoelectric structures with the typical unimorph and bimorph systems. Various theoretical methods have been developed using the circuit technique combinations [34-37], Rayleigh–Ritz methods [38,39], modal analysis methods [40], and the weak-form technique [41], random vibration analysis [42,43], transfer matrix [44], Galerkin approach [45,46], closed-form boundary value methods [47,48], analytical voltage- and charge-type Hamiltonian methods [49], electromechanical finite element analyses [50,51], and the segmented unimorph smart pipe conveying fluid [52]. Another research work focusing on the composite linear multimorph energy harvester [53] has been investigated using the form closed-form distributed parameter. More recently, alternative approach for producing the multi-resonance peaks, using the closed form boundary value method [54,55], impedance analytical method [56] and finite element-based SSHI (synchronized switch harvesting on inductor) approach [57,58], has been investigated by applying a number of the piezoelectric beam arrays. This strategy allows the power harvesting levels to adapt with the ambient vibration that changes over time. In recent research works, triggering the multi-resonance peaks using a single piezoelectric bimorph beam with distributed system can also be achieved by applying the shunt control-based electrode configurations [59,60]. This tuning strategy allows one layer of the smart beam acting as the shunt control with passive electrical network to boost another layer for generating the power harvesting. Different tuning response system using the smart plate, controlled by the multi-segment array with the on-off switching techniques, has been developed using electromechanical finite element analysis [61]. The multi-tuning system provides an effective tool to adaptively control the level of power output and frequency domain where it depends on switching certain active segments of smart plate.

As reported in the literature reviews, the two previous research studies of the smart structures have shown examples of the potential engineering applications. Although these two areas are mostly investigated independently, the power harvesting- and shunt control-based discontinuous smart structures with the non-homogeneous system provide a direct benefit for effectively widening and tuning the multi-resonances with adaptive response system. Unlike the previous works, the major contributions of the proposed work can be highlighted as follows:

1. The constitutive coupled equations using full variational parameters have been derived simultaneously using the charge type-based Hamiltonian mechanics and the Ritz method-based weak-form analytical approach. These parameters consist of all parametric harvesting and shunt circuits, mechanical system of elasticity with mechanical stress-strain and dynamic motions, and electromechanical system of electrical displacement, electrical stress and electric-polarity field. Note that only key formulations are given for presenting the technical concept of the proposed study.
2. The accuracy of the theoretical method provides faster convergence while only using lower number of mode iteration or degree of freedom. The convergence study has been conducted using the iterative computational process of the optimal frequency response with full coupled electromechanical system parameters.
3. The three types of discontinuous laminated smart beams with non-homogeneous system have been discussed showing the different levels of electromechanical effect on the harvested power and tuning ability. Type-1 is the segmented smart beam with the PZN-PT materials for both tuning and harvesting layers. Type-2 uses the PZT PSI-5A4E for tuning layer and the PZN-PT for harvesting layer. Type-3 uses the PZT PSI-5A4E for both tuning and harvesting layers. Each smart structural systems are connected with the shunt circuit and AC–DC circuit interfaces.
4. The structural system model can give more efficient and practical in creating the transverse flexibility. It also potentially reduces the cost of using the piezoelectric materials. The proposed adaptive structural system can be important to practically fit the vibration environment that sometimes changes over time.
5. Further parametric studies have been explored to identify the wider shift of the two resonances of the optimal power output frequencies, while only using the first mode of the smart structure. Moreover, the appearance or disappearance of the two-equal peak at the first resonance and/or the second resonance may potentially occur at the optimal response, showing the level of the electromechanical effect. This phenomenon shows a proof in which its relevancy was derived explicitly by [36]. Detail discussions of the adaptive optimal energy harvesting have also been presented using the parametric shunt circuit tuning.

2 Physical System

In Fig. 1, discontinuous laminated smart beam with non-homogeneous system and proof mass offset is subjected to the base excitation. This system model consists of the two segments. The first segment is used for harvesting piezoelectric components connected with the AC-DC harvesting circuit. The second segment is used for the tuning piezoelectric system connected with the shunt circuit. Moreover, the first and second segments provide the three and two layers, respectively. The middle layer is the passive substructure. At this case, the asymmetric neutral axes at the both segments are different. The point of attachment for the proof mass whose the centroid has a distance offset to the end of the system model obviously depends on the asymmetric neutral axis at the second segment. These issues will affect the dynamic equations of the system model. As shown here for a modelling example, the series connection at the first segment appears to be a bimorph system. In general, when the piezoelectric element undergoes transverse input base motion as assumed here, the upper and lower layers of the piezoelectric bimorph can respectively deform with the tension and

compressive strains and vice versa where the polarisation of the upper layer will then create opposite directions compared with the lower layer. Under repetitive deformations, the AC signal from the piezoelectric layers can be generated and converted to the DC signal via a full-bridge rectifier with the smoothing RC circuit.

It is important to note here that the bimorph system at the first segment is not restricted on having the similar material and equal thickness between lower and upper layers of the piezoelectric components. For many previous works with the distributed piezoelectric structure (continuous system), the electric fields of bimorph system with the series and parallel connections are considered to multiply by factors of half and one for each piezoelectric layer, respectively. Also, the sign conventions of the electric field and polarisation for the series and parallel bimorph configurations have also been developed in detail [62-64], where the piezoelectric coupling and internal capacitance of the total piezoelectric layers of the symmetrical bimorph system were aimed to be calculated separately from the constitutive dynamic equations. As a result, the piezoelectric coupling and internal capacitance for the series bimorph gave half and one-fourth of the parallel bimorph, respectively. However, this paper is not restricted by all of the aforementioned points. The reason is that the proposed technique obviously underlies on the simultaneous derivations by taking into account all aspects of the physical systems and circuit analysis using the charge type-based Hamiltonian mechanics. The key formulations of the coupled system model as a whole will be expressed in the forthcoming section.

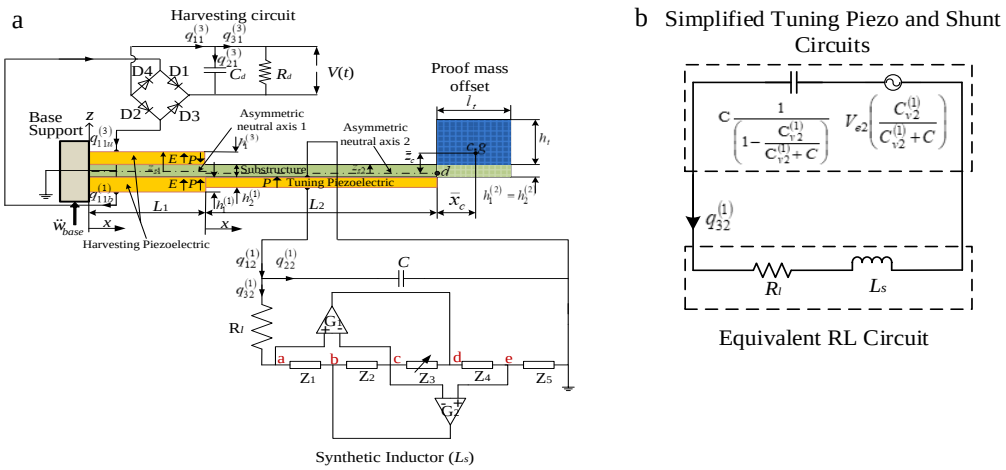

Fig.1. Smart structural system with offset proof mass under base excitation with harvesting and tuning circuits: a) physical system, b) equivalent tuning piezoelectric circuit and tuning shunt circuit

3 Electromechanical Weak Form Analytical Approach

A new development of the analytical method for the nonhomogeneous and discontinuous smart structure with proof mass offset is developed in this section. It combines the tuning and harvesting circuits, mechanical system (elasticity with mechanical stress and dynamic motions) and electromechanical system (electrical displacement, electrical stress and electric-polarity field).

3.1 Formulations of fully coupled equations

The coupled dynamic system of the discontinuous smart beam with the integrated piezoelectric energy harvesting and shunt control can be formulated using the extended charge type-based Hamiltonian mechanics [49], giving,

$$\left.\int_{t_1}^{t_2} \delta\left(L_a + W_f\right)\mathrm{d}t = 0 \;\right\} \begin{array}{l} L_a \in \{KE, PE, WE, WC, WL\} \\ W_f \in \{WF, WR\} \end{array} , \tag{1}$$

or

$$\int_{t_1}^{t_2} \left(\delta KE - \delta PE - \delta WE + \delta WF - \delta WC + \delta WL + \delta WR\right)\mathrm{d}t = 0 . \tag{2}$$

Each functional energy form in Eq. (2) can be expressed briefly in Appendix A. Note that since the given expressions of energy forms were formulated in terms of the nonhomogeneous and discontinuous cantilever smart beam with proof mass offset, they therefore are different to those shown in [59-60]. The variational forms of the given functional energy expressions can be prescribed as the continuous differentiable functions of virtual displacements, electric displacements and charges for the whole system that can be stated as,

$$L_a = L_a\left(\begin{array}{l} \dot{w}(x,t),\ \dot{w}(L_2,t),\ \dfrac{\partial \dot{w}(L_2,t)}{\partial x},\ \dfrac{\partial^2 w(x,t)}{\partial x^2}, \\ D_3^{(1)}(z,t), D_3^{(3)}(z,t),\ q_{22}^{(1)}(t), q_{21}^{(3)}(t), q_{32}^{(1)}(t) \end{array}\right), \tag{3.1}$$

$$W_f = W_f\left(w(x,t), \frac{\partial w(L_2,t)}{\partial x}, w(L_2,t), q_{32}^{(1)}(t), q_{31}^{(3)}(t)\right) . \tag{3.2}$$

Applying total differential equations into Eqs. (3.1) and (3.2) gives,

$$\begin{aligned} \delta L_a = {} & \overbrace{\frac{\partial L_a}{\partial \dot{w}(x,t)}\delta\dot{w}(x,t) + \frac{\partial L_a}{\partial \dot{w}(L,t)}\delta\dot{w}(L_2,t) + \frac{\partial L_a}{\partial\left(\dfrac{\partial \dot{w}}{\partial x}(L_2,t)\right)}\delta\left(\frac{\partial \dot{w}}{\partial x}(L_2,t)\right)}^{\text{Virtual Kinetic Energy based on generalised velocities of elastic structure and proof mass offset}} \\ & + \overbrace{\frac{\partial L_a}{\partial\left(\dfrac{\partial^2 w(x,t)}{\partial x^2}\right)}\delta\left(\frac{\partial^2 w(x,t)}{\partial x^2}\right)}^{\text{Virtual Strain Energy based on generalised mechanical strain}} + \overbrace{\frac{\partial L_a}{\partial D_3^{(1)}(z,t)}\delta D_3^{(1)}(z,t) + \frac{\partial L_a}{\partial D_3^{(3)}(z,t)}\delta D_3^{(3)}(z,t)}^{\text{Virtual Electrical Energy based on generalised electric displacements}} \\ & + \overbrace{\frac{\partial L_a}{\partial q_{22}^{(1)}(t)}\delta q_{22}^{(1)}(t) + \frac{\partial L_a}{\partial q_{21}^{(3)}(t)}\delta q_{21}^{(3)}(t) + \frac{\partial L_a}{\partial q_{32}^{(1)}(t)}\delta q_{32}^{(1)}(t)}^{\text{Virtual Electrical Energy of Harvesting and Tuning Circuits based on generalised electric charges}} , \end{aligned} \tag{4.1}$$

$$\begin{aligned} \delta W_f = {} & \overbrace{\frac{\partial W_f}{\partial w(x,t)}\delta w(x,t) + \frac{\partial W_f}{\partial\left(\dfrac{\partial w}{\partial x}(L_2,t)\right)}\delta\left(\frac{\partial w}{\partial x}(L_2,t)\right) + \frac{\partial W_f}{\partial w(L_2,t)}\delta w(L_2,t)}^{\text{Virtual Work based on generalised displacement of structure and proof masss offset (base excitation)}} \\ & + \overbrace{\frac{\partial W_f}{\partial q_{32}^{(1)}(t)}\delta q_{32}^{(1)}(t) + \frac{\partial W_f}{\partial q_{31}^{(3)}(t)}\delta q_{31}^{(3)}(t)}^{\text{Virtual Work based on generalised electric charges}} . \end{aligned} \tag{4.2}$$

The variational parameters such as the virtual relative transverse displacement field, harvesting electrical charge, and tuning electrical charge are required to formulate the weak-form equation. After manipulation and simplification, the electromechanical weak-form equation of Eq. (2) can be further formulated using the expressions given in Appendix A in terms of Eqs. (4.1)-(4.2) to yield,

$$\begin{aligned}
&\int_{t_1}^{t_2}\Bigg[\int_0^L\sum_{n=1}^{2}H_n(x)\left\{\left(I_{0n}\ddot{w}(x,t)+I_{0n}\ddot{w}_{base}(t)\right)\delta w(x,t)+C_{tn}\frac{\partial^2 w(x,t)}{\partial x^2}\frac{\partial^2\delta w(x,t)}{\partial x^2}\right\}\mathrm{d}x\\
&+\int_0^L\left(\eta_1^{(1)}q_{11b}^{(1)}(t)+\eta_1^{(3)}q_{11u}^{(3)}(t)\right)H_1(x)\frac{\partial^2\delta w(x,t)}{\partial x^2}\mathrm{d}x+\int_0^L\eta_2^{(1)}q_{12}^{(1)}(t)H_2(x)\frac{\partial^2\delta w(x,t)}{\partial x^2}\mathrm{d}x\\
&+H_2(x)\left\{x_cI_0^{tip}\frac{\partial\ddot{w}(L_2,t)}{\partial x}+I_0^{tip}\ddot{w}(L_2,t)+I_0^{tip}\ddot{w}_{base}(t)\right\}\delta w(L_2,t)\\
&+H_2(x)\left\{I_2^{tip}\frac{\partial\ddot{w}(L_2,t)}{\partial x}+x_cI_0^{tip}\ddot{w}(L_2,t)+x_cI_0^{(tip)}\ddot{w}_{base}(t)\right\}\delta\frac{\partial w(L_2,t)}{\partial x}\\
&+\left\{\int_0^L\eta_1^{(1)}\frac{\partial^2 w(x,t)}{\partial x^2}\mathrm{d}x+\frac{q_{11b}^{(1)}(t)}{C_{v1}^{(1)}}\right\}H_1(x)\delta q_{11b}^{(1)}(t)+\left\{\int_0^L\eta_1^{(3)}\frac{\partial^2 w(x,t)}{\partial x^2}\mathrm{d}x+\frac{q_{11u}^{(3)}(t)}{C_{v1}^{(3)}}\right\}H_1(x)\delta q_{11u}^{(3)}(t)\\
&+\left\{\int_0^L\eta_2^{(1)}\frac{\partial^2 w(x,t)}{\partial x^2}\mathrm{d}x+\frac{q_{12}^{(1)}(t)}{C_{v2}^{(1)}}\right\}H_2(x)\delta q_{12}^{(1)}(t)+\left(L_s\ddot{q}_{32}^{(1)}(t)+R_l\dot{q}_{32}^{(1)}(t)\right)\delta q_{32}^{(1)}(t)\\
&+\frac{q_{22}^{(1)}(t)\delta q_{22}^{(1)}(t)}{C}+\frac{q_{21}^{(3)}(t)\delta q_{21}^{(3)}(t)}{C_d}+R_d\dot{q}_{31}^{(3)}(t)\delta q_{31}^{(3)}(t)\Bigg]\,\mathrm{d}t=0\,.
\end{aligned}\tag{5}$$

Some coefficients can be formulated as,

$$\eta_1^{(1)}=\frac{g_{31}^{(1)}\left(h_1^{(1)^2}+2h_1^{(1)}h_1^{(3)}+2h_1^{(2)}h_1^{(1)}-2z_{s1}h_1^{(1)}\right)}{2L_1},\tag{6.1}$$

$$\eta_2^{(1)}=\frac{g_{31}^{(1)}\left(h_2^{(1)^2}+2h_2^{(2)}h_2^{(1)}-2z_{s2}h_2^{(1)}\right)}{2L_2},\quad \eta_1^{(3)}=\frac{g_{31}^{(3)}\left(2z_{s1}h_1^{(3)}-h_1^{(3)^2}\right)}{2L_1},\tag{6.2}$$

$$C_{v1}^{(1)}=\frac{\varepsilon_{33}^{(1,S)}b_1^{(1)}L_1}{h_1^{(1)}},\quad C_{v2}^{(1)}=\frac{\varepsilon_{33}^{(1,S)}b_2^{(1)}L_2}{h_2^{(1)}},\quad C_{v1}^{(3)}=\frac{\varepsilon_{33}^{(3,S)}b_1^{(3)}L_1}{h_1^{(3)}},\tag{6.3}$$

$$I_{0n}=\sum_{i=1}^{m}\rho_n^{(i)}b_n^{(i)}h_n^{(i)}\quad\forall\, n\in\{1,2\},\tag{6.4}$$

$$C_{tn}=\frac{1}{3}\left(\sum_{i=1}^{m}\bar{c}_D^{(i)}b_n^{(i)}\left(\sum_{j=i}^{m}h_n^{(i)}-z_{sn}\right)^3-\sum_{i=1}^{m-1}\bar{c}_D^{(i)}b_n^{(i)}\left(\sum_{j=i+1}^{m}h_n^{(j)}-z_{sn}\right)^3+\bar{c}_D^{(m)}b_n^{(m)}z_{sn}{}^3\right)\forall\, n\in\{1,2\},\tag{6.5}$$

$$z_{sn}=\frac{\sum_{i=1}^{m}\bar{c}_D^{(i)}h_n^{(i)^2}b_n^{(i)}+2\sum_{i=1}^{m-1}\bar{c}_D^{(i)}h_n^{(i)}b_n^{(i)}\sum_{j=i+1}^{m}h_n^{(j)}}{2\sum_{i=1}^{m}\bar{c}_D^{(i)}h_n^{(i)}b_n^{(i)}}\quad\forall\, n\in\{1,2\}\,.\tag{6.6}$$

Note that if the general parameter $\bar{c}_D=\bar{c}_{11}$, it will refer to the non-active layer. Other essential piezoelectric parameters can be defined in Appendix A. Parameter *b* is the width of the interlayer and term *m* is number of layers for each segment (term *n*). The general parameter $H_n(x)$ represents the Heaviside functions.

Applying KCL for the internal piezoelectric connection (series connection) with harvesting circuit and tuning circuit in Fig. 1 gives the electric charge equations,

$$q_{11}^{(3)} = q_{11b}^{(1)} = q_{11u}^{(3)} \quad , \quad q_{11}^{(3)} = q_{21}^{(3)} + q_{31}^{(3)} , \tag{7.1}$$

$$q_{12}^{(1)} = q_{22}^{(1)} + q_{32}^{(1)} . \tag{7.2}$$

The variables $q_{21}^{(3)}$ and $q_{22}^{(1)}$ in Eq. (5) can be eliminated for simplicity using,

$$\frac{q_{21}^{(3)}(t)}{C_d}\delta q_{21}^{(3)}(t) = \frac{q_{11}^{(3)}(t)}{C_d}\delta q_{11}^{(3)}(t) - \frac{q_{31}^{(3)}(t)}{C_d}\delta q_{11}^{(3)}(t) - \frac{q_{11}^{(3)}(t)}{C_d}\delta q_{31}^{(3)}(t) + \frac{q_{31}^{(3)}(t)}{C_d}\delta q_{31}^{(3)}(t) , \tag{8.1}$$

$$\frac{q_{22}^{(1)}(t)}{C}\delta q_{22}^{(1)}(t) = \frac{q_{12}^{(1)}(t)}{C}\delta q_{12}^{(1)}(t) - \frac{q_{32}^{(1)}(t)}{C}\delta q_{12}^{(1)}(t) - \frac{q_{12}^{(1)}(t)}{C}\delta q_{32}^{(1)}(t) + \frac{q_{32}^{(1)}(t)}{C}\delta q_{32}^{(1)}(t) . \tag{8.2}$$

It is important to note that the existence of the parameter in Eq. (8.1) was excluded in the previous works in [59-60]. The capacitance at harvesting circuit was only excluded into the constitutive coupled equations to formulate the frequency response equations. But, it was then derived separately when formulating the signal waveform equations due to complexity of the simultaneous derivations [59-60]. However, as shown in this paper, the overall system model, which is used into the non-homogenous and discontinuous smart beam with variable piezoelectric material, is presented and different from the previous works.

The Ritz method-based weak form [65-67] can be further formulated for the required solution. The method requires a test function which is a piecewise continuous function over the physical domain of the coupled system as a whole. The function must meet continuity requirements and boundary conditions. The normalised eigenfunction series form can be formulated as,

$$w(x,t) = \sum_{r=1}^{m} \hat{W}_r(x) w_r(t) \quad . \tag{9}$$

The first coupled dynamic equation representing the electromechanical system can be formulated by substituting Eq. (9) into Eq. (5), giving,

$$\begin{aligned}
&\sum_{q=1}^{m}\left\{\sum_{r=1}^{m}\left[\left(\int_0^L \sum_{n=1}^{2} I_{0n} H_n(x)\hat{W}_q(x)\hat{W}_r(x)\,\mathrm{d}x + H_2(x)\left(I_0^{tip}\hat{W}_q(L_2)\hat{W}_r(L_2) + x_c I_0^{tip}\hat{W}_q(L_2)\frac{\mathrm{d}\hat{W}_r(L_2)}{\mathrm{d}x}\right.\right.\right.\\
&\left. + x_c I_0^{tip}\frac{\mathrm{d}\hat{W}_q(L_2)}{dx}\hat{W}_r(L_2) + I_2^{tip}\frac{\mathrm{d}\hat{W}_q(L_2)}{\mathrm{d}x}\frac{\mathrm{d}\hat{W}_r(L_2)}{\mathrm{d}x}\right)\ddot{w}_r(t) + \int_0^L \sum_{n=1}^{2} H_n(x)\left(C_{tn}\frac{\mathrm{d}^2\hat{W}_q(x)}{\mathrm{d}x^2}\frac{\mathrm{d}^2\hat{W}_r(x)}{\mathrm{d}x^2}\right)\mathrm{d}x w_r(t)\right.\\
&+\int_0^L\left(\eta_1^{(1)}+\eta_1^{(3)}\right)H_1(x)\frac{\mathrm{d}^2\hat{W}_q}{\mathrm{d}x^2}\mathrm{d}x q_{11}^{(3)}(t) + \int_0^L \eta_2^{(1)} H_2(x)\frac{\mathrm{d}^2\hat{W}_q}{\mathrm{d}x^2}\mathrm{d}x q_{12}^{(1)}(t) + \left(\int_0^L\sum_{n=1}^{2} H_n(x) I_{0n}\hat{W}_q(x)\,\mathrm{d}x\right.\\
&\left.\left.\left. + H_2(x)\left(x_c I_0^{tip}\frac{\mathrm{d}\hat{W}_q(L_2)}{\mathrm{d}x} + I_0^{tip}\hat{W}_q(L)\right)\right)\ddot{w}_{base}(t)\right\}\delta w_q(t) = 0 .
\end{aligned} \tag{10}$$

The second, third, fourth and fifth coupled dynamic equations represent the electromechanical coupling one and two and the harvesting and tuning circuit forms can be formulated respectively as,

$$\left\{\sum_{r=1}^{m}\int_0^L\left(\eta_1^{(1)}+\eta_1^{(3)}\right)H_1(x)\frac{\mathrm{d}^2\hat{W}_r(x,t)}{\mathrm{d}x^2}\mathrm{d}x w_r(t) + \left(\frac{C_{v1}^{(1)}+C_{v1}^{(3)}}{C_{v1}^{(1)}C_{v1}^{(3)}}H_1(x) + \frac{1}{C_d}\right)q_{11}^{(3)}(t) - \frac{q_{31}^{(3)}(t)}{C_d}\right\}\delta q_{11}^{(3)}(\mathrm{t}) = 0 , \tag{11.1}$$

$$\left\{\sum_{r=1}^{m}\int_0^L \eta_2^{(1)}\frac{\mathrm{d}^2\hat{W}_r(x,t)}{\mathrm{d}x^2}\mathrm{d}x w_r+\left(\frac{H_2(x)}{C_{v2}^{(1)}}+\frac{1}{C}\right)q_{12}^{(1)}(t)-\frac{q_{32}^{(1)}(t)}{C}\right\}\delta q_{12}^{(1)}(t)=0 \quad , \tag{11.2}$$

$$\left\{R_d\dot{q}_{31}^{(3)}(t)+\frac{q_{31}^{(3)}(t)}{C_d}-\frac{q_{11}^{(3)}(t)}{C_d}\right\}\delta q_{31}^{(3)}(t)=0\,, \tag{11.3}$$

$$\left\{L_s\ddot{q}_{32}^{(1)}(t)+R_l\dot{q}_{32}^{(1)}(t)+\frac{q_{32}^{(1)}(t)}{C}-\frac{q_{12}^{(1)}(t)}{C}\right\}\delta q_{32}^{(1)}(t)=0\,. \tag{11.4}$$

Eq. (10) and Eqs. (11.1)-(11.4) can be further simplified into matrix form by including the mechanical damping coefficients, giving,

$$\begin{bmatrix} M_{qr} & 0 & 0 \\ 0 & L_s & 0 \\ 0 & 0 & 0 \end{bmatrix}\begin{Bmatrix} \ddot{w}_r \\ \ddot{q}_{32}^{(1)} \\ \ddot{q}_{31}^{(3)} \end{Bmatrix}+\begin{bmatrix} C_{qr} & 0 & 0 \\ 0 & R_l & 0 \\ 0 & 0 & R_d \end{bmatrix}\begin{Bmatrix} \dot{w}_r \\ \dot{q}_{32}^{(1)} \\ \dot{q}_{31}^{(3)} \end{Bmatrix}+\begin{bmatrix} K_{qr}-\tilde{P}_{1q}\tilde{P}_{1r}\gamma C_d-\tilde{P}_{2q}\tilde{P}_{2r}\mu C & \tilde{P}_{2q}\mu & \tilde{P}_{1q}\gamma \\ \tilde{P}_{2r}\mu & P_C & 0 \\ \tilde{P}_{1r}\gamma & 0 & P_{Cd} \end{bmatrix}\begin{Bmatrix} w_r \\ q_{32}^{(1)} \\ q_{31}^{(3)} \end{Bmatrix}=\begin{Bmatrix} -Q_q\ddot{w}_{base}(t) \\ 0 \\ 0 \end{Bmatrix}, \tag{12}$$

where $M_{qr}=\int_0^L\sum_{n=1}^{2}I_{0n}H_n(x)\hat{W}_q(x)\hat{W}_r(x)\mathrm{d}x+I_0^{tip}H_2(x)\hat{W}_q(L_2)\hat{W}_r(L_2)$

$$+H_2(x)\left(x_cI_0^{tip}\hat{W}_q(L_2)\frac{\mathrm{d}\hat{W}_r(L_2)}{\mathrm{d}x}+x_cI_0^{tip}\frac{\mathrm{d}\hat{W}_q(L_2)}{\mathrm{d}x}\hat{W}_r(L_2)+I_2^{tip}\frac{\mathrm{d}\hat{W}_q(L_2)}{\mathrm{d}x}\frac{\mathrm{d}\hat{W}_r(L_2)}{\mathrm{d}x}\right), \tag{13.1}$$

$$C_{qr}=c_vM_{qr}+c_dK_{qr}\ , \tag{13.2}$$

$$K_{qr}=\int_0^L\sum_{n=1}^{2}C_{tn}H_n(x)\frac{\mathrm{d}^2\hat{W}_q(x)}{\mathrm{d}x^2}\frac{\mathrm{d}^2\hat{W}_r(x)}{\mathrm{d}x^2}\mathrm{d}x\,, \tag{13.3}$$

$$\tilde{P}_{1r}=\int_0^L\left(\eta_1^{(1)}+\eta_1^{(3)}\right)H_1(x)\frac{\mathrm{d}^2\hat{W}_r(x)}{\mathrm{d}x^2}\mathrm{d}x\ ,\quad \tilde{P}_{1q}=\int_0^L\left(\eta_1^{(1)}+\eta_1^{(3)}\right)H_1(x)\frac{\mathrm{d}^2\hat{W}_q(x)}{\mathrm{d}x^2}\mathrm{d}x\ , \tag{13.4}$$

$$\tilde{P}_{2r}=\int_0^L\eta_2^{(1)}H_2(x)\frac{\mathrm{d}^2\hat{W}_r(x)}{\mathrm{d}x^2}\mathrm{d}x\ ,\tilde{P}_{2q}=\int_0^L\eta_2^{(1)}H_2(x)\frac{\mathrm{d}^2\hat{W}_q(x)}{\mathrm{d}x^2}\mathrm{d}x\ , \tag{13.5}$$

$$\mathrm{P_C}=\frac{1}{C}(1-\mu)\quad ,\quad \mu=\frac{C_{v2}^{(1)}}{\left(C_{v2}^{(1)}+C\right)}\,, \tag{13.6}$$

$$P_{Cd}=\frac{1}{C_d}(1-\gamma)\,,\quad \gamma=\frac{C_{v1}^{(1)}C_{v1}^{(3)}}{\left(C_{v1}^{(1)}C_d+C_{v1}^{(3)}C_d+C_{v1}^{(1)}C_{v1}^{(3)}\right)}\,, \tag{13.7}$$

$$Q_q=\int_0^L\sum_{n=1}^{2}I_{0n}H_n(x)\hat{W}_q(x)\mathrm{d}x+H_2(x)\left(I_0^{tip}\hat{W}_q(L_2)+x_cI_0^{tip}\frac{\mathrm{d}\hat{W}_q(L_2)}{\mathrm{d}x}\right). \tag{13.8}$$

3.2 Identification of the exact solution-based Ritz eigenfunctions

Parameter normalised eigenfunction $\hat{W}_\mathrm{r}(.)$ from Eq. (9) can be proved as,

$$\hat{W}_r(x)=\frac{W_r(x)}{\left(\int_0^L\sum_{n=1}^{2}I_{0n}H_n(x)W_r(x)^2\,\mathrm{d}x+H_2(x)\left(I_0^{tip}W_r(L_2)^2+2x_cI_0^{tip}W_r(L_2)\frac{\mathrm{d}W_r}{\mathrm{d}x}(L_2)+I_2^{tip}\left(\frac{\mathrm{d}W_r}{\mathrm{d}x}(L_2)\right)^2\right)\right)^{1/2}}\ ,r=1,2,..,\ m\,, \tag{14}$$

where the non-normalised $W_\mathrm{r}(.)$ can be obtained from the generalised space-dependent Ritz eigenfunctions as,

$$W_r\left(x\right) = \sum_{k=1}^{m} c_{kr} W_k\left(x\right) \ , \ r = 1,2,....,m \quad . \tag{15}$$

Note that the accuracy of the non-normalised Ritz mode shape $W_k\left(x\right)$ can be obtained using the closed-form boundary value technique where it can be found in the next stage. The generalised Ritz coefficient c_{kr} is the eigenvector matrix where each column corresponds to a specific independent eigenvalue. The coefficient can only be obtained by replacing Eq. (9) with $w(x,t) = \sum_{r=1}^{m} c_r W_r\left(x\right) e^{i\omega t}$ and rearranging Eq. (5) by considering only the characteristic mechanical equation giving, $\sum_{r=1}^{m}\left[\bar{K}_{qr} - \omega^2 \bar{M}_{qr}\right] c_r = 0$, $q = 1,2,....,m$. Parameters $\bar{K}_{qr}$ and $\bar{M}_{qr}$, whose values depend on $W_k\left(x\right)$, are the non-normalised forms, and different with the normalised forms as given in Eqs. (13.1) and (13.3). Once the Ritz coefficient data sets of column vector are collected, they can be transformed into the matrix form ($c_r \to c_{kr}$). The following procedure is used to obtain $W_k\left(x\right)$ from Eq. (15) where the accuracy of the non-normalised Ritz eigenfunctions can be used for formulating the eigenfrequency and eigenmode solutions. Note that these exact solutions can be obtained by extending Eq. (2) to particularly formulate the strong-form analytical models in order to obtain the closed-form boundary value equations, and the result of which can be further reduced by applying the variational method of duBois-Reymond's theorem. After simplification, the mechanical dynamic equations for the nonhomogeneous and discontinuous laminated smart beam with proof mass offset can be formulated as,

$$I_{01}\ddot{w}_1\left(x,t\right) + C_{t1}\frac{\partial^4 w_1\left(x,t\right)}{\partial x^4} = 0 \ , \quad I_{02}\ddot{w}_2\left(x,t\right) + C_{t2}\frac{\partial^4 w_2\left(x,t\right)}{\partial x^4} = 0 \quad . \tag{16}$$

The static boundary conditions are given as,

$$w_1\left(0,t\right) = 0 \ , \quad \frac{\partial w_1\left(0,t\right)}{\partial x} = 0 \ . \tag{17}$$

The transition boundary conditions are shown as,

$$w_1\left(L_1,t\right) = w_2\left(0,t\right), \quad \frac{\partial w_1\left(L_1,t\right)}{\partial x} = \frac{\partial w_2\left(0,t\right)}{\partial x} \ , \tag{18.1}$$

$$C_{t1}\frac{\partial}{\partial x}\left(\frac{\partial^2 w_1\left(L_1,t\right)}{\partial x^2}\right) = C_{t2}\frac{\partial}{\partial x}\left(\frac{\partial^2 w_2\left(0,t\right)}{\partial x^2}\right), \quad C_{t1}\frac{\partial^2 w_1\left(L_1,t\right)}{\partial x^2} = C_{t2}\frac{\partial^2 w_2\left(0,t\right)}{\partial x^2} \ . \tag{18.2}$$

The dynamic boundary conditions can be formulated as,

$$x_c I_0^{tip}\frac{\partial \ddot{w}_2\left(L_2,t\right)}{\partial x} + I_0^{tip}\ddot{w}_2\left(L_2,t\right) - C_{t2}\frac{\partial}{\partial x}\left(\frac{\partial^2 w_2\left(L_2,t\right)}{\partial x^2}\right) = 0 \ , \tag{19.1}$$

$$I_2^{tip}\frac{\partial \ddot{w}_2\left(L_2,t\right)}{\partial x} + x_c I_0^{tip}\ddot{w}_2\left(L_2,t\right) + C_{t2}\frac{\partial^2 w_2\left(L_2,t\right)}{\partial x^2} = 0 \ . \tag{19.2}$$

It is clearly seen that the extra parameters from the offset proof mass contributes into Eqs. (19.1)-(19.2). The method of separation of variables for each segment was used by substituting $w_1\left(x,t\right) = W_{k1}\left(x\right) y_1\left(t\right)$ and $w_2\left(x,t\right) = W_{k2}\left(x\right) y_2\left(t\right)$ into Eq. (16). As mentioned previously, since the mode shapes for each segment as shown in Fig. 1 are required by Eq. (15), the following general solutions of $W_{k1}\left(x\right)$ and $W_{k2}\left(x\right)$ can be formulated as,

$$W_k(x)=\begin{cases} W_{k1}(x) = A_1\cos\mu x + B_1\sin\mu x + C_1\cosh\mu x + D_1\sinh\mu x \ , \ 0\le x\le L_1 \\ W_{k2}(x) = A_2\cos\beta x + B_2\sin\beta x + C_2\cosh\beta x + D_2\sinh\beta x \ , \ 0\le x\le L_2 \end{cases} . \tag{20}$$

Using Eq. (20) into Eqs. (17)-(19), the characteristic equations in the matrix form can be formulated, giving,

$$\begin{bmatrix} a_{11} & a_{12} & a_{13} & a_{14} & a_{15} & a_{16} & a_{17} & a_{18} \\ a_{21} & a_{22} & a_{23} & a_{24} & a_{25} & a_{26} & a_{27} & a_{28} \\ a_{31} & a_{32} & a_{33} & a_{34} & a_{35} & a_{36} & a_{37} & a_{38} \\ a_{41} & a_{42} & a_{43} & a_{44} & a_{45} & a_{46} & a_{47} & a_{48} \\ a_{51} & a_{52} & a_{53} & a_{54} & a_{55} & a_{56} & a_{57} & a_{58} \\ a_{61} & a_{62} & a_{63} & a_{64} & a_{65} & a_{66} & a_{67} & a_{68} \\ a_{71} & a_{72} & a_{73} & a_{74} & a_{75} & a_{76} & a_{77} & a_{78} \\ a_{81} & a_{82} & a_{83} & a_{84} & a_{85} & a_{86} & a_{87} & a_{88} \end{bmatrix} \begin{Bmatrix} A_1 \\ B_1 \\ C_1 \\ D_1 \\ A_2 \\ B_2 \\ C_2 \\ D_2 \end{Bmatrix} = 0 . \tag{21}$$

Each element of the matrix in Eq. (21) can be seen in Appendix C. As shown in Eq. (20), the two dependent parameters $\mu = \sqrt[4]{\omega^2 I_{01}/C_{t1}}$ and $\beta = \sqrt[4]{\mu^4 I_{02}C_{t1}/(I_{01}C_{t2})}$ exist where these obviously depend on the natural frequency ω of the system (eigenvalue). Next, Eq. (21) must satisfy the nontrivial solution for $|\boldsymbol{a}_{nm}| = 0$, leading to the frequency equation. But $\boldsymbol{a}_{nm}$ still contains dependent parameters μ, β, and ω. It must be modified first by showing only a single input parameter. One of the options is that β and ω can be replaced using the above relation μ. At this case, whatever the value μ is iteratively chosen, the computational process of the frequency equation must be equal to zero, showing the eigenvalue related to the particular mode number. Once the proper values μ for any mode numbers are obtained, other values β and ω can subsequently be calculated. The eigenmode from Eq. (20) with the constants (A_1, B_1, C_1, D_1; A_2, B_2, C_2, D_2) can then be solved as shown in Appendix C where the updated constants clearly depend on the matrix elements of $\boldsymbol{a}_{nm}$ or the parameters μ, β, and ω.

3.3 Solutions of fully coupled dynamic equations

The orthonormalisations can now be further proved using Eq. (14) and applying the orthogonality property of the mechanical dynamic equations as,

$$\int_0^L \sum_{n=1}^{2} I_{0n}H_n(x)\hat{W}_q(x)\hat{W}_r(x)\,\mathrm{d}x + H_2(x)\Bigg(I_0^{tip}\hat{W}_q(L_2)\hat{W}_r(L_2) + x_c I_0^{tip}\hat{W}_q(L_2)\frac{\mathrm{d}\hat{W}_r(L_2)}{\mathrm{d}x}$$
$$+ x_c I_0^{tip}\frac{\mathrm{d}\hat{W}_q(L_2)}{\mathrm{d}x}\hat{W}_r(L_2) + I_2^{tip}\frac{\mathrm{d}\hat{W}_q(L_2)}{\mathrm{d}x}\frac{\mathrm{d}\hat{W}_r(L_2)}{\mathrm{d}x}\Bigg) = \delta_{qr} = \begin{cases} 0 & if \ \ r\ne q \\ 1 & if \ \ r = q \end{cases} , \tag{22.1}$$

$$\int_0^L \sum_{n=1}^{2} C_{tn}H_n(x)\frac{\mathrm{d}^2\hat{W}_q(x)}{\mathrm{d}x^2}\frac{\mathrm{d}^2\hat{W}_r(x)}{\mathrm{d}x^2}\,\mathrm{d}x = \delta_{qr}\omega_r^{\ 2} = \begin{cases} 0 & if \ \ r\ne q \\ \omega_r^{\ 2} & if \ \ r = q \end{cases} . \tag{22.2}$$

where δ_{qr} is the Kronecker delta, defined as unity for $q = r$ and zero for $q \ne r$. Note that parameters $\hat{W}_r(x)$ and $\hat{W}_q(x)$ indicate normalised mode shapes. Applying the orthonormalisations from Eq. (22) into Eq. (12) gives,

$$\ddot{w}_r(t) + 2\zeta_r\omega_r\dot{w}_r(t) + \left(\omega_r^{\ 2} - \hat{\tilde{P}}_{1r}\tilde{P}_{1r}\gamma C_d - \hat{\tilde{P}}_{2r}\tilde{P}_{2r}\mu C\right)w_r(t) + \tilde{P}_{2r}\mu q_{32}^{(1)}(t) + \tilde{P}_{1r}\gamma q_{31}^{(3)}(t) = -Q_q\ddot{w}_{base}(t) , \tag{23.1}$$

$$L_s\ddot{q}_{32}^{(1)}(t) + R_1\dot{q}_{32}^{(1)}(t) + P_C q_{32}^{(1)}(t) + \hat{\tilde{P}}_{2r}\mu w_r(t) = 0 , \tag{23.2}$$

$$R_d \dot{q}_{31}^{(3)}(t) + P_{Cd} q_{31}^{(3)}(t) + \hat{\tilde{P}}_{1r} \gamma w_r(t) = 0 \quad . \tag{23.3}$$

As can be seen, the three coupled equations are formulated showing dependable relations to each other. The equations can be further formulated into FRFs as shown in the stage. Moreover, the FRFs provide accurate results as long as the test function-based Ritz eigenfunction is chosen correctly. At this case, since Eq. (23) has been normalised, the modified parameters can be formulated as,

$$\tilde{P}_{1r} = \left(\eta_1^{(1)} + \eta_1^{(3)}\right) \frac{\mathrm{d}\hat{W}_r(L_1)}{\mathrm{d}x}, \quad \tilde{P}_{2r} = \eta_2^{(1)} \left(\frac{\mathrm{d}\hat{W}_r(L_2)}{\mathrm{d}x}\right), \quad \hat{\tilde{P}}_{1r} = \sum_{r=1}^{m} \tilde{P}_{1r}, \quad \hat{\tilde{P}}_{2r} = \sum_{r=1}^{m} \tilde{P}_{2r} . \tag{24}$$

Note that other parameters can be seen in Eq. (13). Laplace transformation can be used to formulate the multi-mode electromechanical FRFs equations giving the transfer functions. Here only one example of the harvesting electrical power FRF is shown across the load resistance after simplification,

$$\frac{q_{31}^{(3)}(j\omega)}{-\omega^2 w_{base} e^{j\omega t}} = \frac{\sum_{r=1}^{m} \frac{Q_r \tilde{P}_{1r} \gamma}{\tilde{N}_r \tilde{G}}}{1 - \sum_{r=1}^{m} \frac{\tilde{P}_{1r}^2 \gamma^2}{\tilde{N}_r \tilde{G}} - \sum_{r=1}^{m} \frac{\tilde{P}_{2r}^2 \mu^2}{\tilde{N}_r \tilde{E}}}, \tag{25}$$

where

$$\tilde{N}_r = \omega_r^2 - \tilde{P}_{1r}^2 \gamma C_d - \tilde{P}_{2r}^2 \mu C - \omega^2 + j 2\zeta_r \omega_r \omega , \tag{26.1}$$

$$\tilde{E} = P_C - L_s \omega^2 + j\omega R_l , \quad \tilde{G} = P_{Cd} + j\omega R_d . \tag{26.2}$$

As shown in Eq. (25), the voltage-charge relation across the resistor or capacitor of the harvesting circuit [49] can be used to calculate the FRF as,

$$\frac{v(j\omega)}{-\omega^2 w_{base} e^{j\omega t}} = j\omega R_d \frac{q_{31}^{(3)}(j\omega)}{-\omega^2 w_{base} e^{j\omega t}} \quad . \tag{27}$$

Also, the power-charge relation across the resistor and capacitor [49] can be used respectively to calculate the FRFs as,

$$\frac{P_{\mathrm{Res}}(j\omega)}{\left(-\omega^2 w_{base} e^{j\omega t}\right)^2} = -\omega^2 R_d \frac{q_{31}^{(3)}(j\omega)^2}{\left(-\omega^2 w_{base} e^{j\omega t}\right)^2} \quad , \tag{28.1}$$

$$\frac{P_{Cap}(j\omega)}{\left(-\omega^2 w_{base} e^{j\omega t}\right)^2} = -j\omega^3 R_d^2 C_d \frac{q_{31}^{(3)}(j\omega)^2}{\left(-\omega^2 w_{base} e^{j\omega t}\right)^2} \quad . \tag{28.2}$$

After simplification, the optimal load resistance can be formulated using Eq. (28.1), giving,

$$R_d^{opt} = \left| -\frac{j}{\omega} \left(P_{Cd} - \frac{\sum_{r=1}^{m} \frac{\tilde{P}_{1r}^2 \gamma^2}{\tilde{N}_r}}{\left(1 - \sum_{r=1}^{m} \frac{\tilde{P}_{2r}^2 \mu^2}{\tilde{N}_r \tilde{E}}\right)} \right) \right| \quad . \tag{29}$$

3.4 Harvesting AC-DC Interface Circuit.

The electrical waveforms from AC to DC signals as shown in Fig. 2 can be generated from harvesting circuit due to the smart system under dynamic excitation. Note that the process of capturing these signals obviously depends upon the control system from the piezoelectric tuning layer with shunt circuit component as shown in Fig. 1. Here, the AC-DC full bridge rectifier and smoothing

RC circuit are utilised, and the process of the voltage and current output signals at the interface circuit can be seen in [36,59]. With this process, the time-waveform signal repeats continuously, provided that the smart system is subject to the excitation.

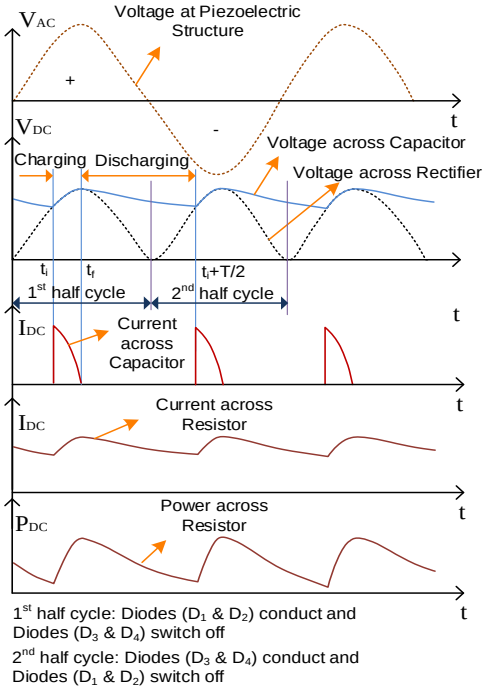

Fig.2. Time waveforms of the harvesting circuit

a. Current flowing with interval $t_i < t < t_f$ indicating the charging time over every half-cycle of the frequency.

As shown at the previous equations, the coupled system can be formulated using Eq. (23) with slight modification in Eq. (23.1). The fourth and seventh terms of Eq. (23.1) were removed. The first term of Eq. (23.3) was also replaced by v_d. Note that this process can also be alternatively proved using modifications of the previous parts with Hamiltonian equations. Here, the following equations during the period of charging can be reformulated as,

$$\ddot{w}_r(t) + 2\zeta_r\omega_r\dot{w}_r(t) + \left(\omega_r^2 - \hat{\tilde{P}}_{2r}\tilde{P}_{2r}\mu C\right)w_r(t) + \tilde{P}_{2r}\mu q_{32}^{(1)}(t) + \tilde{P}_{1r}q_{11}^{(3)}(t) = -Q_q\ddot{w}_{base}(t), \tag{30.1}$$

$$L_s\ddot{q}_{32}^{(1)}(t) + R_1\dot{q}_{32}^{(1)}(t) + P_C q_{32}^{(1)}(t) + \hat{\tilde{P}}_{2r}\mu w_r(t) = 0, \tag{30.2}$$

$$v_d + P_V^{(3)}q_{11}^{(3)}(t) + \hat{\tilde{P}}_{1r}w_r(t) = 0 \quad . \tag{30.3}$$

where $P_V^{(3)} = \left(C_{v1}^{(1)} + C_{v1}^{(3)}\right)\Big/C_{v1}^{(1)}C_{v1}^{(3)}$. Differentiating Eq. (30.3) with respect to time gives,

$$\dot{v}_d + P_V^{(3)}\dot{q}_{11}^{(3)}(t) + \hat{\tilde{P}}_{1r}\dot{w}_r(t) = 0. \tag{31}$$

The equation for the harvesting circuit using the KCL equation can be formulated as,

$$\dot{q}_{11}^{(3)}(t) - C_d\dot{v}_d - \frac{v_d}{R_d} = 0. \tag{32}$$

Substituting parameter $q_{11}^{(3)}(t)$ from Eq. (30.3) into Eq. (30.1) and parameter $\dot{q}_{11}^{(3)}$ from (31) into Eq. (32), the state space equation can be formulated as,

$$
\frac{\mathrm{d}}{\mathrm{d}t}\begin{Bmatrix} w_1 \\ w_2 \\ \cdot \\ \cdot \\ w_r \\ \dot{w}_1 \\ \dot{w}_2 \\ \cdot \\ \cdot \\ \dot{w}_r \\ q_{32}^{(1)} \\ \dot{q}_{32}^{(1)} \\ v_d \end{Bmatrix} = \begin{bmatrix}
\dot{w}_1 \\ \dot{w}_2 \\ \cdot \\ \cdot \\ \dot{w}_r \\
-2\zeta_1\,\omega_1\,\dot{w}_1 - \omega_1^{\,2}\,w_1 + \hat{\tilde{P}}_{21}\tilde{P}_{21}\mu C w_1 - \tilde{P}_{21}\mu q_{32}^{(1)}(t) + \dfrac{\sum_{r=1}^{m}\tilde{P}_{1r}\tilde{P}_{1r}w_r}{P_V^{(3)}} + \dfrac{\tilde{P}_{11}v_d}{P_V^{(3)}} - Q_1\,\ddot{w}_{base}(t) \\
-2\zeta_2\,\omega_2\,\dot{w}_2 - \omega_2^{\,2}w_2 + \hat{\tilde{P}}_{22}\tilde{P}_{22}\mu C w_2 - \tilde{P}_{22}\mu q_{32}^{(1)}(t) + \dfrac{\sum_{r=1}^{m}\tilde{P}_{1r}\tilde{P}_{1r}w_r}{P_V^{(3)}} + \dfrac{\tilde{P}_{12}v_d}{P_V^{(3)}} - Q_2\,\ddot{w}_{base}(t) \\
\cdot \\ \cdot \\
-2\zeta_r\,\omega_r\,\dot{w}_r - \omega_r^{\,2}w_r + \hat{\tilde{P}}_{2r}\tilde{P}_{2r}\mu C w_r - \tilde{P}_{2r}\mu q_{32}^{(1)}(t) + \dfrac{\sum_{r=1}^{m}\tilde{P}_{1r}\tilde{P}_{1r}w_r}{P_V^{(3)}} + \dfrac{\tilde{P}_{1r}v_d}{P_V^{(3)}} - Q_r\,\ddot{w}_{base}(t) \\
\dot{q}_{32}^{(1)} \\
-\dfrac{R_l\,\dot{q}_{32}^{(1)}}{L_s} - \dfrac{P_C\,q_{32}^{(1)}}{L_s} - \dfrac{\sum_{r=1}^{m}\tilde{P}_{2r}\mu w_r}{L_s} \\
-\dfrac{\sum_{r=1}^{m}\tilde{P}_{1r}\dot{w}_r}{\left(P_V^{(3)}C_d + 1\right)} - \dfrac{v_d}{\left(R_d\,C_d + \dfrac{R_d}{P_V^{(3)}}\right)}
\end{bmatrix}. \tag{33}
$$

b. Current flowing with interval $t_f < t < t_i + T/2$ indicating the discharging times every half-cycle of the frequency.

For this process, the harvesting circuit becomes $C_d\dot{v}_d + v_d/R_d = 0$, and its solution gives,

$$
v_d(t) = v_d(t_f)\exp\left(\frac{-(t - t_f)}{C_d R_d}\right). \tag{34}
$$

The collection of the time waveform signal data using Eqs. (33) and (34) can be utilised to estimate the current and voltage waveform during the charging and discharging periods. The basic formulas of the DC currents across the resistor and capacitor and DC power output across the resistor as shown in Fig. 2 can be stated respectively as,

$$
I_{DC\_R_d} = \frac{v_d}{R_d},\ I_{DC\_C_d} = \dot{v}_d C_d,\ \ P_{p\_R_d} = v_d I_{DC\_R_d}. \tag{35}
$$

Note that the parameter $\dot{v}_d$ at DC signal output in Eq. (35) can be formulated, giving,

$$
\dot{v}_d = \left| -\frac{\sum_{r=1}^{m}\tilde{P}_{1r}\dot{w}_r}{\left(P_V^{(3)}C_d + 1\right)} - \frac{v_d}{\left(R_d\,C_d + \dfrac{R_d}{P_V^{(3)}}\right)} \right| = \begin{cases} -\dot{v}_d & \text{if } \dot{v}_d < 0 \\ \dot{v}_d & \text{if } \dot{v}_d \geq 0 \end{cases}. \tag{36}
$$

4 Results and Discussions

This section discusses parametric studies of the shunt vibration energy harvesting control of discontinuous piezoelectric beam structure with proof mass offset using the optimal power output frequency and time waveform responses. At this case, three types of the discontinuous smart beam structures with different piezoelectric materials were utilised to explore the adaptive power harvesting. These types of the smart system can be seen in Table 1. The material properties of the smart beam are given in Table 2. Note that the physical system used here is still the same model as shown in Fig. 1. The geometry parameters of length L, width b and substructure thickness $h^{(2)}$ were set to 60 mm, 6 mm, and 0.5 mm, respectively. Other thickness parameters for piezoelectric segments of both tuning and harvesting layers were set to be variable. The base excitation of the physical system was set to 1 m/s^2. Note that each selected piezoelectric thickness was utilised for both segments. Also each segment (L_1 and L_2) for the smart beam was equally set to 30 mm. The steel proof mass offset with l_t, h_t and b (width) were set to 15 mm, 10 mm and 6 mm, respectively.

Table 1. Types of discontinuous smart beams

Segments	Type-1	Type-2	Type-3
Tuning piezoelectric	PZN-PT	PZT PSI-5A4E	PZT PSI-5A4E
Harvesting piezoelectric	PZN-PT	PZN-PT	PZT PSI-5A4E

Table 2. Material properties

Material properties	PZT PSI-5A4E	PZN-PT	Brass
Young's modulus, $\bar{c}_{11}$ (GPa)	66	25	105
Density, ρ (kg/m^3)	7800	8000	9000
Piezoelectric constant, d_{31} (pm/V)	-190	-1200	-
Permittivity, ε_{33}^T (F/m)	1800 ε_o	6500 ε_o	-
permittivity of free space, ε_o (pF/m)	8.854	8.854	-

Fig. 3 shows the optimal power output frequency response based on number of mode iteration. This is an example of the appearance of the two resonances at the first mode using Type-1. It is clearly seen that faster convergence of the frequency response can be achieved using lower number of mode iteration or degree of freedom. Note that the optimal power output is calculated using the optimal harvesting load resistance where it is shown in Eqs. (28.1) and (29). As shown, using m=3 and m=4,

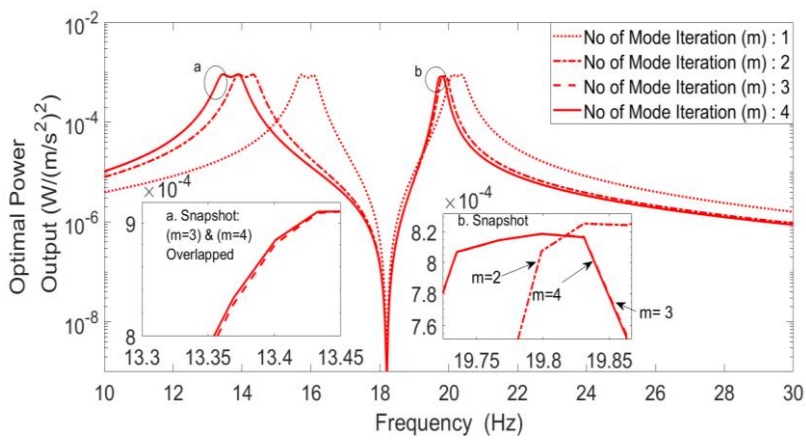

Fig. 3. Convergence study using optimal power output FRFs with the piezoelectric thickness of 0.197 mm, tuning capacitor C=150 nF, harvesting capacitor C_d =0.1 μF, tuning resistor R_l=50 Ω, and synthetic inductance L_s=450 H.

the results tend to favorably overlap each other. The reason is that the Ritz eigenfunctions were iterated using the exact solution of the system model. Note that all results displayed at the next stage are based on the first mode of the smart structure systems. But, the iterative computational process for the frequency analyses was obviously conducted using the exact four-mode approximation.

In Fig 4, by varying the piezoelectric thickness for each type of discontinuous smart beam, the optimal power outputs at the first mode of the smart structure systems are shown with the two resonances using optimal tuning inductance value. It should also be noted that the results shown in Fig. 4 is based on the optimal synthetic inductance where its value depends upon the tuning circuit resonance and tuning capacitance. It was obtained from Eq. 35.2, giving the parameter $L_s = P_C / \omega_r^{\ 2}$. It is clearly seen that the parameter will vary if the piezoelectric thickness changes. Note that the piezoelectric material also produces an inherent capacitance depending on its thickness. Therefore, the optimal synthetic inductance varies according to the size of those thickness parameters. If the resonance of the tuning circuit is chosen to be a similar value to that of the resonance of the smart structure, the result will give the lowest power amplitude, and it will not be applicable for the power harvesting system, but rather for vibration suppression [59]. Here, the optimal synthetic inductances used in Fig. 3 only become a reference so as to further identify a stimulus to the adaptive response of the power harvesting. However, further results of the system response will be elaborated in the next stage using the variable tuning synthetic inductance, load resistance and capacitance. The effect of the two resonances at the first mode occurs due to the combination between the electromechanical system and tuning circuit. This phenomenon shows relevancy in [36] with different model of analysis. In specific case, Type-1 and -2 in Figs. 3a and b obviously show the two-equal peak of the first resonance due to using the optimal harvesting load resistances. It means that if certain harvesting load resistance values are chosen to plot the power frequency responses, each resonance of those responses will coincide well with the optimal responses. Note that the appearance of two-equal peak occurs due to the existence of strong electromechanical effect from the PZN-PT structure segment. Those equal peaks representing the lower and higher resonances are sometime called the short- and open-circuit resonances, respectively. The phenomenon of the two-equal peak as proposed by [36] was also proved here. In [36], the explicit equations were derived to show the short- and open-circuit resonances. The electromechanical effect is mainly affected by the piezoelectric coupling and capacitance and the load resistance. As shown in Table 2, the PZN-PT has higher piezoelectric constant and permittivity compared with the PZT PSI-5A4E. Note that both segments of Type-1 use PZN-PT materials with variable piezoelectric thickness, giving the strongest electromechanical effect as shown in wider bandwidths of the two-equal peak. This indicates that Type-3 gives the weakest electromechanical effect and the lowest amplitude. Note that Type-1 and -2 with the piezoelectric thicknesses of 0.197 mm and 0.267 mm give effective options for the system model because they show wider bandwidths of the two-equal peak. Also, majority of the piezoelectric thicknesses for Type-1 and -2 show higher amplitudes for both resonances. This occurs because the system model was affected by the shunt piezoelectric segment for tuning the frequency response. At this point, the piezoelectric thickness of 0.197 mm will be further used for analysis as shown in the next stage. The appearance of these resonances can be important response to practically fit the vibration environment that sometimes changes over time.

Here, example of another result related to the variable smart beam length based on the Type-1 was added in order to show different dynamic behaviour. First, the different thicknesses of piezo layer (Fig. 4) or different length of smart beam (Fig.5) can affect the calculations of the internal capacitance and electromechanical coupling of piezoelectric component for producing the power output in the frequency domain. Second, the increasing thickness of piezo layer can directly affect the characteristic mechanical transverse dynamics of the structure itself for shifting the resonances from lower to higher values due to the predominant increase of its stiffness that can create the overall structure to be stiffer. In opposite phenomenon, the increasing smart beam length can result in the decrease of resonance frequency due to the predominant decrease of its stiffness that can create the overall structure to be more flexible.

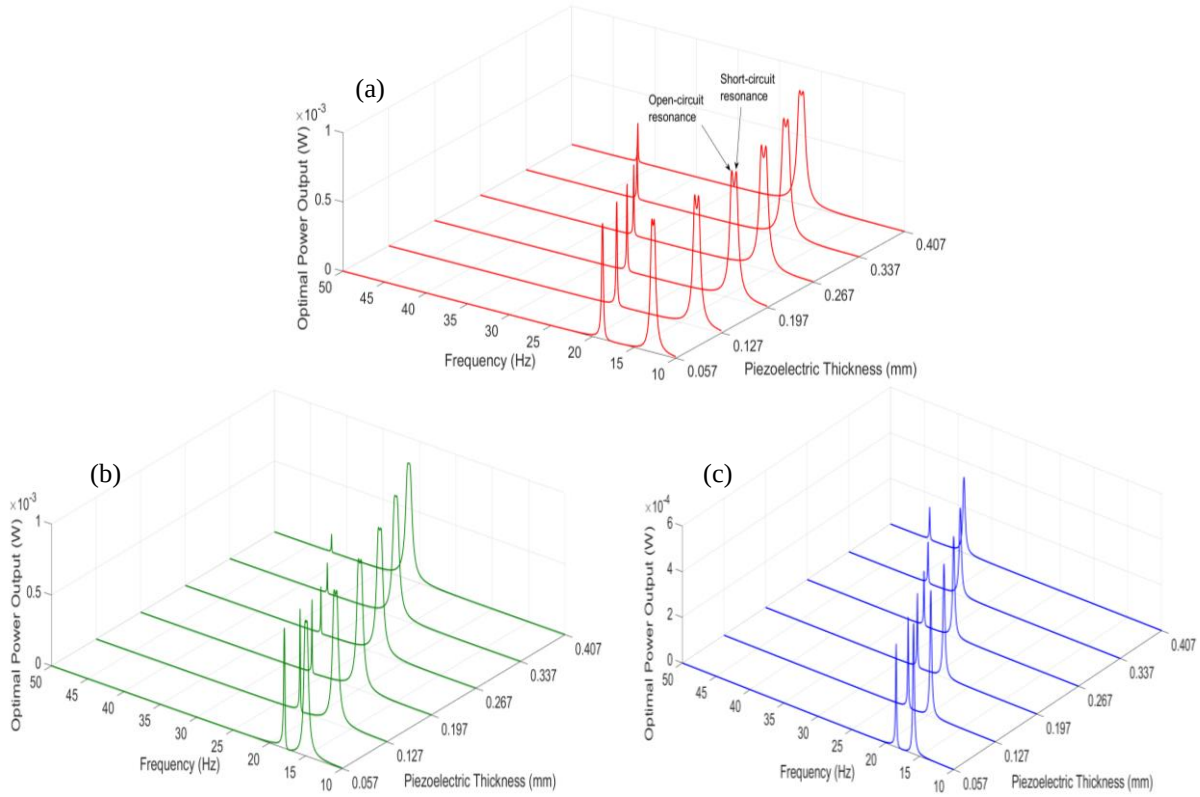

Fig. 4. Optimal Power harvesting FRFs with variable piezoelectric thickness using tuning capacitor C=60 nF, harvesting capacitor C_d =0.1 μF, tuning resistor R_l=50 Ω, and variable optimal synthetic inductance: a) Type-1, b) Type-2, c) Type-3.

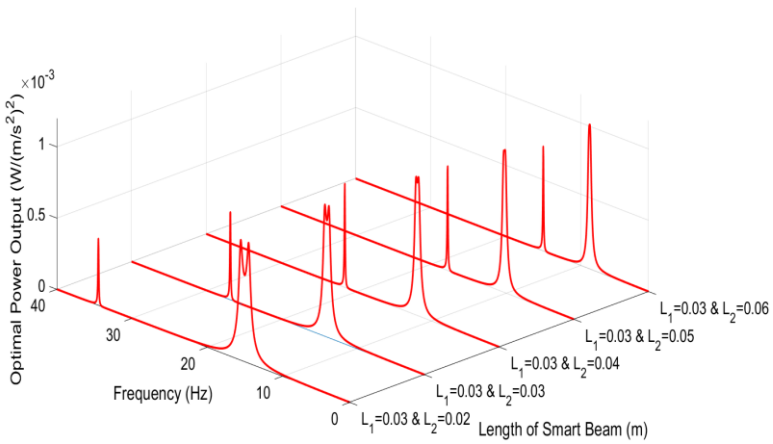

Fig. 5. Optimal Power harvesting FRFs for Type-1 with variable smart beam length using tuning capacitor C=60 nF, harvesting capacitor C_d =0.1 μF, tuning resistor R_l=50 Ω, and variable optimal synthetic inductance.

Also, although discontinuous smart beam model gives more complex system compared with the distributed model, it can reduce the cost of using the piezoelectric material and provide the ease of a transverse flexibility to vibrate under base excitation.

In Fig. 6, the two resonances of the optimal power outputs using the three types of discontinuous smart beams generally appear to form different trends. Note that each type has three figures with three different capacitance values. The optimal power outputs with a wider resonance band occur when the synthetic inductance changes. It clearly shows that wider shift occurs for all three types. However, the Type-1 provides the most responsive shift for tuning the frequencies of the optimal power output, followed by Type-2 and Type-3. The optimal configurations depend on the physical properties and geometry of the piezoelectric components at both segments and the use of the harvesting and tuning circuits. For example, using harvesting capacitor C_d =0.1 μF, tuning resistor R_l=50 Ω, and tuning capacitor C=60 nF, Figs. 6a, d and g under variable tuning inductance show different shift patterns of the optimal response.

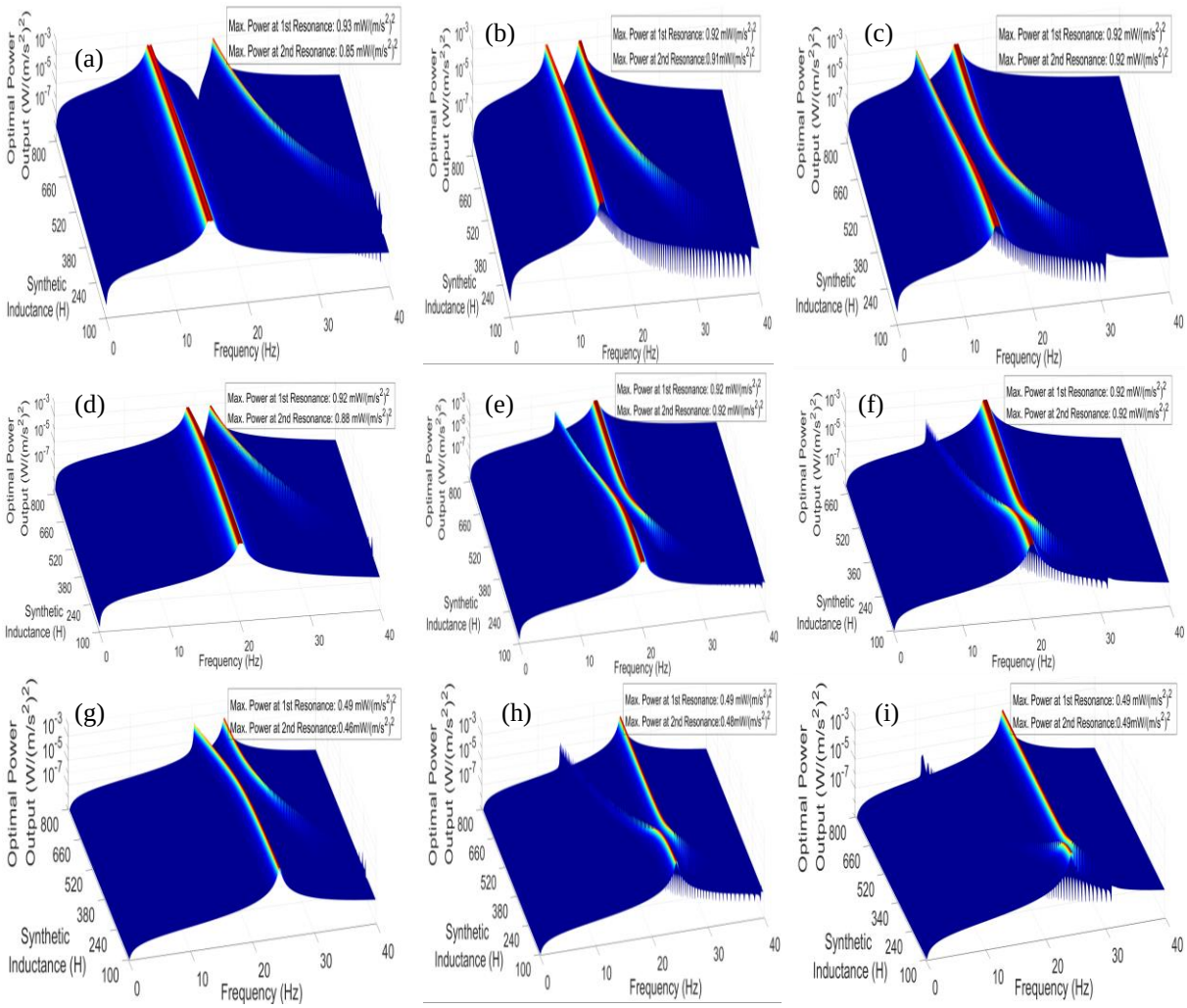

Fig. 6. Optimal Power harvesting FRFs with piezoelectric thickness of 0.197 mm using harvesting capacitor C_d =0.1 μF, tuning resistor R_l=50 Ω, and variable synthetic inductance : a) Type-1 with tuning capacitor C=60 nF,, b) Type-1 with tuning capacitor C=150 nF, c) Type-1 with tuning capacitor C=250 nF, d) Type-2 with tuning capacitor C=60 nF, e) Type-2 with tuning capacitor C=150 nF , f) Type-2 with tuning capacitor C=250, g) Type-3 with tuning capacitor C=60 nF, h) Type-3 with tuning capacitor C=150 nF, i) Type-3 with tuning capacitor C=250 nF.

In specific case, Figs. 6a-c show the sequence of the system responses for the Type-1 using different tuning capacitances where the shift of the second resonance appears to be more responsive compared with the first resonance peak under variable synthetic inductance. Only Fig. 6c provides a slighter shift at the first resonance. If the synthetic inductance increases further from its current maximum point as shown, the first resonance will also turn to be a wider shift in the system response. For the Type-2, slightly different optimal power output response, particularly shown in Figs. 6e-f, gives a moderate shift for both resonances using variable the synthetic inductance. Moreover, the two resonances for the Type-3 give a slower responsive shift as shown in Figs. 6g-I and provide a lower power output. It is important to note that the wider shift of the first and second resonances and higher power output using moderate synthetic inductance values provide effective response to the adaptive tuning energy harvesting. Example can be found at the Type-1 and -2. The two-equal peaks of the first or/and second resonance/s for the Type-1 and -2 also exists using variable synthetic inductance. Fig. 6a clearly shows these peaks, particularly at the first resonance.

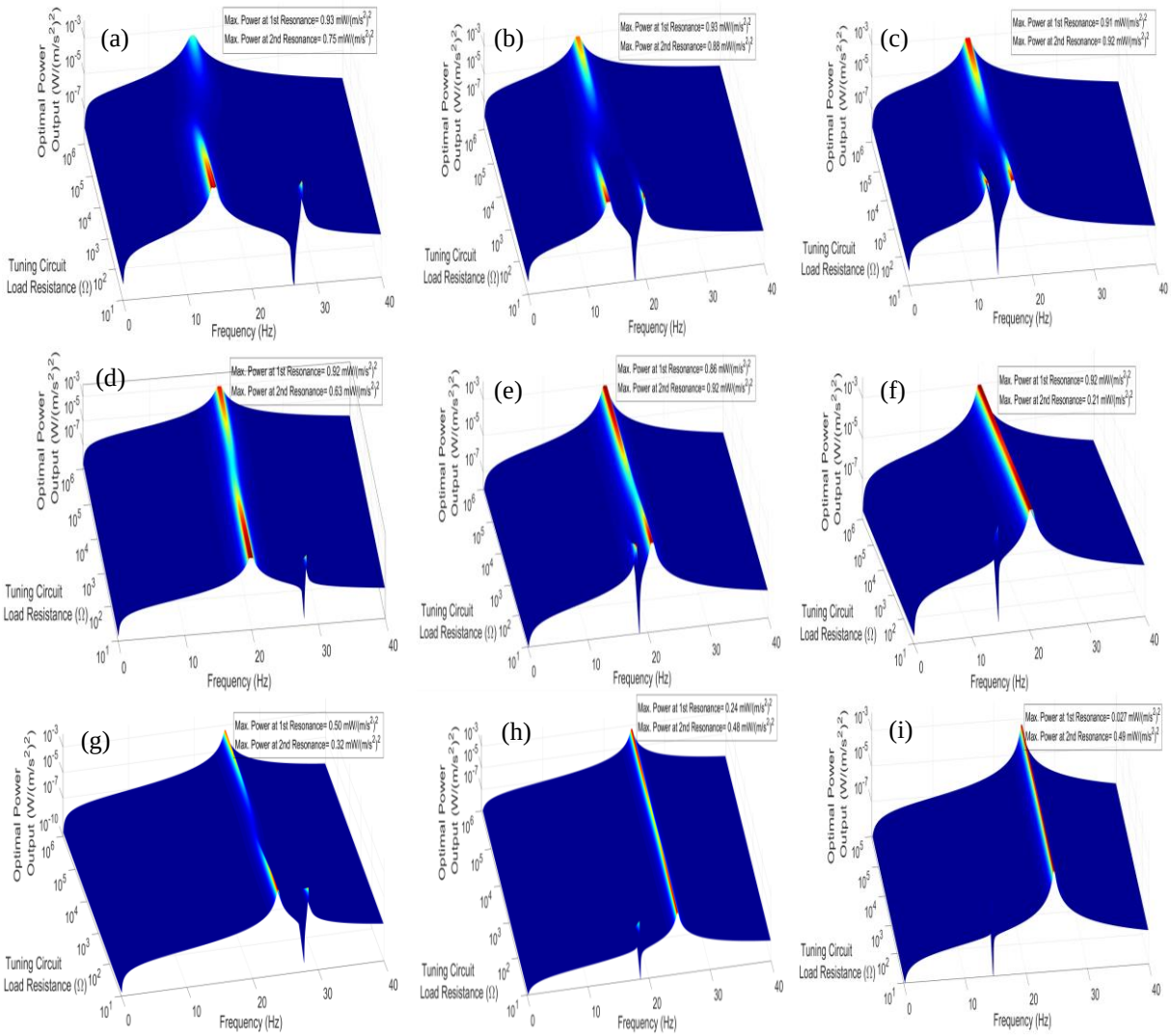

Fig. 7. Optimal Power harvesting FRFs with piezoelectric thickness of 0.197 mm using harvesting capacitor C_d =0.1 μF, synthetic inductance L_s=450 H, and variable tuning resistor: a) Type-1 with tuning capacitor C=60 nF,, b) Type-1 with tuning capacitor C=150 nF, c) Type-1 with tuning capacitor C=250 nF, d) Type-2 with tuning capacitor C=60 nF, e) Type-2 with tuning capacitor C=150 nF , f) Type-2 with tuning capacitor C=250, g) Type-3 with tuning capacitor C=60 nF, h) Type-3 with tuning capacitor C=150 nF, i) Type-3 with tuning capacitor C=250 nF.

However, when the tuning capacitance changes as shown in Figs. 6b-c, the first and second resonances show the two-equal peak, particularly at the lower and higher synthetic inductance values, respectively. The similar event also occurs in Fig. 4a-c, but shows different parametric studies. In particular, the two-equal peak at both resonances begins to occur at the lower and moderate larger synthetic inductances, respectively.

Unlike the tuning response as shown in Fig. 6, the optimal powers with variable tuning load resistance using the three types show different trends as given in Fig. 7. In general, all of the results with the appearance of the two and single resonances occur at the lower and higher tuning load resistances, respectively. Also, it indicates that the system response with the lower tuning load resistance, as approaching to the short circuit, provides to form the two resonances. The existence of the single resonance can be triggered by the open circuit load resistance at the tuning circuit. The existence of the two resonances also occurs due to using the short circuit load resistance at the tuning circuit. The two resonances at the lower tuning load resistances become closer each other due to using the three different capacitance values. For specific case as shown Figs. 7a-c, the Type-1 provides different system responses when using the three different tuning capacitance values. It also shows that the resonance peaks predominantly appear at the lower and higher tuning load resistances. This indicates that disappearance of the resonance peaks of the optimal power output occurs at the moderate range of the tuning load resistance values. Again, the two-equal peak at the first resonance also appears in Fig. 7a. Then the two-equal peak in Fig. 7c turns to appear at the second resonance using the lower tuning load resistance. But, when the tuning load resistance approaches to open circuit, the two-equal peak also appears at the single resonance. For the Type-2, the predominant resonance peaks also appear at the lower tuning load resistances as shown in Figs. 7d-f. At the moderate range of the tuning load resistance values, the resonance of the optimal power output still appears with a slight drop, particularly shown in Figs. 7d-e. Here, the two-equal peak also appears as shown in the thick red region. For the Type-3 as shown in Figs. 7g-i, the optimal power outputs at the resonance region seem to give lower responsive compared with the results given from Type-1 and -2. As shown at the Type-3, the thin red region at the resonance response shows lower frequency bandwidth without the two-equal peak.

The visualisations of the time waveform signals of the DC electrical voltage and power outputs at the harvesting circuit are shown using variable frequency excitation, and example is given in Figs. 8 and 9. As previously noted, the Type-1 and -2 show effective adaptive energy harvesters with wider shift of the first and second resonances and higher power outputs. Here, the Type-1 was taken as an example for further analysis. In application, the typical forward voltage drop of the silicon diode is about 0.7V. Since we used a full-bridge AC-DC rectifier by assuming no losses, the forward voltage drop across diode pair $(2\times 0.7V)$ was ignored. The voltage drop across diode occurs due to the intrinsic property of diode having depletion zone at the *p-n* junction and the heat dissipation. In particular, the heat dissipation occurs due to the increase of electric current flowing through the diode. For the piezoelectric harvesting device as a source of AC voltage, the electric current is very low due to high impedance of transducer. But, the generated voltage is high. In [58], the ideal power obtained from the theoretical calculation and the actual power with consideration of the electric loss obtained from the experiment were considered at the diode pair where the efficiency of the system ($P_{\text{exp}}/P_{\text{ideal}}$) is

around 80-85%. But from the purpose of providing the essential guidelines for the system, we can always perform the analysis without considering this loss effect. As shown in Fig. 8a, the DC voltages across the rectifier and capacitor show different levels of amplitudes. It is clearly seen that the DC voltage outputs at particular two frequency excitations also appear the two maximum amplitudes when the tuning load resistance approaches the short-circuit. These frequency excitations obviously approach the resonance regions. The previous results with the frequency response systems have proved this behaviour. It intuitively predicts that when the tuning load resistance changes until approaching the open-circuit, the DC voltage outputs only show a single maximum point where this phenomenon was obviously proved in Fig. 7. The DC voltages at rectifier with different frequency excitations show a larger ripple voltage due to intrinsic signal pattern of full-bridge system for converting the AC signal for every half-circle. But, the ripple voltage can reduce significantly using smoothing RC circuit that can give the benefit for charging and discharging processes for every half-cycle. The trend of DC power outputs in Fig. 9 also shows a similar pattern with the two maximum amplitudes. The results shown here were based on the chosen tuning inductance and capacitance values.

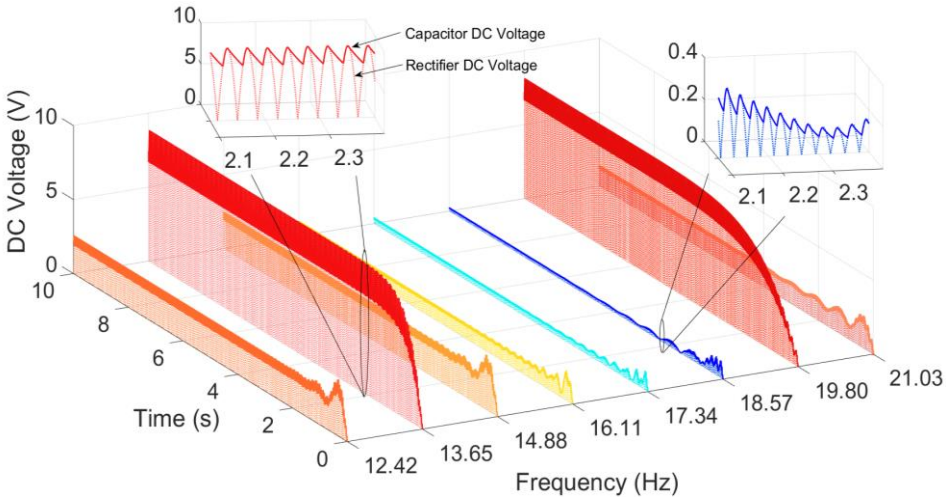

Fig. 8. DC voltage time waveform signals using Type-1 with piezoelectric thickness of 0.197 mm under frequency excitations with the harvesting capacitance C_d=0.1μF, harvesting resistor R_d=100 kΩ, tuning resistor R_l=50 Ω, tuning capacitance C=150 nF, and synthetic inductance L_s=450 H.

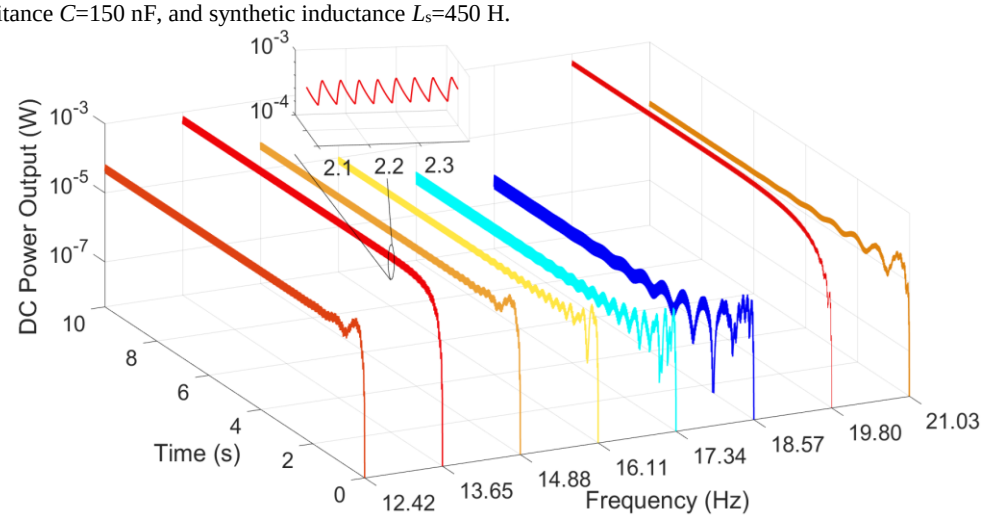

Fig. 9. DC power output time waveform signals using Type-1 piezoelectric thickness of 0.197 mm under frequency excitations with the harvesting capacitance C_d=0.1μF, harvesting resistor R_d=100 kΩ, tuning resistor R_l=50 Ω, tuning capacitance C=150 nF, and synthetic inductance L_s=450 H.

By viewing Fig. 6b, the range of the resonance frequencies at 450 H and 150 nF also proves the system response behaviour. If the tuning inductance with the same capacitance increases further, the frequency excitations to induce the two maximum amplitudes of DC power output as shown in Fig. 9 will give a slight narrow. But, at certain points, these two amplitudes will turn to wider response. Again, whatever the ripple signal from the DC voltage output is generated, it will affect the fluctuation of DC power across load resistance. It is important to note here, the DC power output depends on the parametric identification not only of the harvesting circuit (rectifier and smoothing RC circuit) in general, but also of the tuning circuit which is capable of controlling the system response of DC signal itself.

5 Conclusion

This paper has presented adaptive optimal power harvesting system responses using discontinuous piezoelectric beam structures connected with shunt circuit network and AC-DC harvesting circuit. The constitutive coupled equations with full variational parameters have been formulated using charge-type Hamiltonian method and the Ritz method-based weak-form analytical approach. The accuracy of Ritz eigenfunctions for the system model with proof mass offset was based on the formulation of the exact eigenmode solution. All the results were based on the first mode of the smart structure systems. But, the iterative computational process was obviously conducted using the exact four-mode approximation. As shown, three different types of discontinuous laminated smart beams have been discussed using the variable shunt circuit parameter. For many case scenarios of the vibration analysis including smart structure power harvesting, it is impossible to have the appearance of two resonances under the first mode. In particular, both resonances are quite far away each other showing the region of the short- and open-circuit resonances for the smart beam operated under the first mode. However, the inclusion of the shunt circuit network makes it possible as shown in this paper. Each type of the smart structure provided the optimal system responses with the ability for widening the multi-resonances. However, it was found that the Type-1 and -2 showed higher responsive systems to give the wider shift of the first and second resonances and generate higher optimal power output. But, the wider shift of the two resonances depended on the variable tuning inductance and capacitance. Also, the appearance of the two resonances at the first mode occurred when the tuning load resistance was set to lower value as approaching short circuit. For the optimal power output response, the two-equal peak of the first or/and second resonance/s for the Type-1 and -2 also existed using variable tuning inductance and capacitance. The technique of the two-equal peak as proposed by [36] was also proved and adopted here with more specific case of the proposed study. The appearance of two-equal peak occurred due to the existence of strong electromechanical effect from the PZN-PT structure segment. Those equal peaks representing the lower and higher resonances [36] were sometimes called the short- and open-circuit resonances, respectively. The electromechanical effect was mainly affected by the piezoelectric coupling and capacitance and load resistance. DC time waveform signal outputs with variable frequency excitation also proved that the system response can be triggered by using the shunt control. The two maximum DC voltage and power amplitudes also appeared when particular two frequency excitations approached the resonance regions. But again, the appearance of those maximum amplitudes occurred due to the effect of the

tuning load resistance approaching the short-circuit. Moreover, the shift level between the two frequency excitations for triggering the maximum amplitudes also relied on the chosen tuning inductance and capacitance values.

Appendix A. Functional energy expressions for the nonhomogeneous and discontinuous cantilever smart beam with proof mass offset

The kinetic energy of the system model can be formulated as,

$$\int_{t_1}^{t_2} \delta KE = \int_{t_1}^{t_2} \left\{ \int_0^L \left(\sum_{n=1}^{2} H_n(x) I_{0n} \dot{w}(x,t) \delta \dot{w}(x,t) \right) \mathrm{d}x + H_2(x) \left(I_0^{tip} \dot{w}(L_2,t) \delta \dot{w}(L_2,t) \right.\right.$$
$$\left.\left. + I_2^{tip} \dot{\theta}(L_2,t) \delta \dot{\theta}(L_2,t) + I_0^{tip} x_c \left(\dot{w}(L_2,t) \delta \dot{\theta}(L_2,t) + \dot{\theta}(L_2,t) \delta \dot{w}(L_2,t) \right) \right) \right\} \mathrm{d}t \ . \tag{A1}$$

Parameter I_{0n} represent the zeroth mass moment of inertia of the segmented structures whereas parameters I_0^{tip} and I_2^{tip} represent the zeroth and second mass moments of the proof mass offset. Also note that details of the mathematical expressions for the dynamical structure and proof mass offset as shown in Eq. (A1) can be found in [51]. They were reduced since the relative displacement $w(x,t)$ is defined as the difference between the absolute displacement $w_{abs}(x,t)$ and the base excitation $w_{base}(t)$. Based on the physical geometry in Fig. 1, Heaviside functions for $H_1(x)=H(x)-H(x-L_1)$ and $H_2(x)=H(x)-H(x-L_2)$ are introduced to model the two segmented structures with different mode shapes along the x-axis.

For formulating the strain energy of the laminated structure, the physical system consists of the three piezoelectric layers (the two layers for harvesting circuit in the first segment and one layer for shunt control in the second segment) and one substructure in the second layer. Here, the piezoelectric constitutive equations based on Helmholtz free energy can be formulated in terms of stress-electric field relations [68-69] as,

$$T_1^{(i_1)} = \bar{c}_D^{(i_1)} S_1^{(i_1)} - g_{31}^{(i_1)} D_3^{(i_1)}, \quad E_3^{(i_1)} = -g_{31}^{(i_1)} S_1^{(i_1)} + \varepsilon_{33}^{(i_1,S)^{-1}} D_3^{(i_1)} \ . \tag{A2}$$

$$T_1^{(i_2)} = \bar{c}_D^{(i_2)} S_1^{(i_2)} - g_{31}^{(i_2)} D_3^{(i_2)}, \quad E_3^{(i_2)} = -g_{31}^{(i_2)} S_1^{(i_2)} + \varepsilon_{33}^{(i_2,S)^{-1}} D_3^{(i_2)} \ . \tag{A3}$$

where the general parameters T, S, E and D represent stress, strain, electric field, and electric displacement, respectively. Note that the superscripts $i_1 \in \{1,3\}$ and $i_2 \in \{1\}$ specifically refer to the harvesting and tuning piezoelectric layers located at the first and second segments, respectively. The general coefficients c_D, g and ε indicate modified elastic constant and modified piezoelectric constant, and permittivity at constant strain respectively. The general strain field $S_1(x,t) = -z\,\partial^2 w(x,t)/\partial x^2$ can be used for each layer and the substructure stress form can be stated as $T_1^{(2)} = \bar{c}_{11}^{(2)} S_1^{(2)}$. The modified elastic constant and modified piezoelectric constant for the harvesting and tuning piezoelectric layers can be formulated, respectively as,

$$\bar{c}_D^{(i_1)} = \bar{c}_{11}^{(i_1,E)} + e_{31}^{(i_1)^2} \varepsilon_{33}^{(i_1,S)^{-1}}, \quad g_{31}^{(i_1)} = \varepsilon_{33}^{(i_1,S)^{-1}} e_{31}^{(i_1)}, \tag{A4}$$

$$\bar{c}_D^{(i_2)} = \bar{c}_{11}^{(i_2,E)} + e_{31}^{(i_2)^2} \varepsilon_{33}^{(i_2,S)^{-1}}, \quad g_{31}^{(i_2)} = \varepsilon_{33}^{(i_2,S)^{-1}} e_{31}^{(i_2)} \ . \tag{A5}$$

Note that the parameter $\varepsilon_{33}^{(i_1,S)}$ indicates the permittivity at constant strain (superscript *S*) that can be further formulated as $\varepsilon_{33}^{(i_1,S)} = \varepsilon_{33}^{(i_1,T)} - e_{31}^{(i_1)} d_{31}^{(i_1)}$ where $\varepsilon_{33}^{(i_1,T)}$ is the permittivity at constant stress (superscript *T*). The general parameter e_{31} is piezoelectric coefficient which is obtained using $e_{31} = d_{31}\bar{c}_{11}^{E}$. The similar form can also be applied to the parameters at the tuning piezoelectric layer with the superscript $i_2 \in \{1\}$.

The total strain energy of the system model can be stated as,

$$PE = \frac{1}{2}\sum_{l_1=1}^{3}\int_0^{L_1}\int_{A^{(l_1)}} S_1^{(l_1)} T_1^{(l_1)} \mathrm{d}A^{(l_1)}\mathrm{d}x + \frac{1}{2}\sum_{l_2=1}^{2}\int_0^{L_2}\int_{A^{(l_2)}} S_1^{(l_2)} T_1^{(l_2)} \mathrm{d}A^{(l_2)}\mathrm{d}x \quad . \tag{A6}$$

The variation of the total strain energy in Eq. (A6) can be further formulated as,

$$\int_{t_1}^{t_2}\delta PE\,\mathrm{d}t = \int_{t_1}^{t_2}\left\{\int_0^{L}\sum_{n=1}^{2} H_n(x) C_{tn}\frac{\partial^2 w(x,t)}{\partial x^2}\delta\frac{\partial^2 w(x,t)}{\partial x^2}\mathrm{d}x + \sum_{l_1\in\{1,3\}}\int_0^{L}\int_{A^{(l_1)}} z g_{31}^{(l_1)} D_3^{(l_1)} H_1(x)\delta\frac{\partial^2 w(x,t)}{\partial x^2}\mathrm{d}A^{(l_1)}\mathrm{d}x \right.$$
$$\left. + \sum_{l_2\in\{1\}}\int_0^{L}\int_{A^{(l_2)}} z g_{31}^{(l_2)} D_3^{(l_2)} H_2(x)\delta\frac{\partial^2 w(x,t)}{\partial x^2}\mathrm{d}A^{(l_2)}\mathrm{d}x \right\}\mathrm{d}t \ . \tag{A7}$$

Parameter C_{tn} represents the arbitrary stiffness coefficient of the segmented structures. Note that the general parameter D_3 in (A7) can be modified for the use in the forthcoming reduced dynamic equations. For the first segment, that can give $D_3^{(1)} = q_{11b}^{(1)} \big/ \left(b^{(1)} L_1\right)$ and $D_3^{(3)} = q_{11u}^{(3)} \big/ \left(b^{(3)} L_1\right) \ \forall H_1(x)$. For the second segment, that can become $D_3^{(1)} = q_{12}^{(1)} \big/ \left(b^{(1)} L_2\right) \ \forall H_2(x)$.

The electrical energy term for the piezoelectric layers for the first and second segments can be formulated to give,

$$WE = \frac{1}{2}\sum_{l_1\in\{1,3\}}\int_0^{L_1}\int_{A^{(l_1)}} E_3^{(l_1)} D_3^{(l_1)}\mathrm{d}A^{(l_1)}\mathrm{d}x + \frac{1}{2}\sum_{l_2\in\{1\}}\int_0^{L_2}\int_{A^{(l_2)}} E_3^{(l_2)} D_3^{(l_2)}\mathrm{d}A^{(l_2)}\mathrm{d}x \quad . \tag{A8}$$

Eq. (A8) can be extended and simplified using Eqs. (A2)-(A3) as,

$$\int_{t_1}^{t_2}\delta WE\,\mathrm{d}t = \int_{t_1}^{t_2}\left\{\sum_{l_1\in\{1,3\}}\int_0^{L}\int_{A^{(l_1)}}\left(z g_{31}^{(l_1)}\delta\frac{\partial^2 w(x,t)}{\partial x^2} + \varepsilon_{33}^{(l_1,S)^{-1}} D_3^{(l_1)}\right) H_1(x)\delta D_3^{(l_1)}\mathrm{d}A^{(l_1)}\mathrm{d}x \right.$$
$$\left. + \sum_{l_2\in\{1\}}\int_0^{L}\int_{A^{(l_2)}}\left(z g_{31}^{(l_2)}\delta\frac{\partial^2 w(x,t)}{\partial x^2} + \varepsilon_{33}^{(l_2,S)^{-1}} D_3^{(l_2)}\right) H_2(x)\delta D_3^{(l_2)}\mathrm{d}A^{(l_2)}\mathrm{d}x \right\}\mathrm{d}t \ . \tag{A9}$$

The non-conservative work on the system due to the input base excitation can be stated as,

$$\int_{t_1}^{t_2}\delta WF\mathrm{d}t = \int_{t_1}^{t_2}\left\{-\int_0^{L}\sum_{n=1}^{2} H_n(x) I_{0n}\delta w(x,t)\mathrm{d}x - I_0^{tip} x_c H_2(x)\delta\theta(L_2,t) - I_0^{tip} H_2(x)\delta w(L_2,t)\right\}\ddot{w}_{base}(t)\mathrm{d}t \ . \tag{A10}$$

The electrical energy of the capacitor in terms of the tuning circuit can be formulated as,

$$\delta WC = \frac{1}{C} q_{22}^{(1)}(t)\delta q_{22}^{(1)}(t) + \frac{1}{C_d} q_{21}^{(3)}(t)\delta q_{21}^{(3)}(t) \ . \tag{A11}$$

The electrical work dissipated by the resistor can be stated as,

$$\delta WR = -R_l \dot{q}_{32}^{(1)}(t)\delta q_{32}^{(1)}(t) - R_d \dot{q}_{31}^{(3)}(t)\delta q_{31}^{(3)}(t). \tag{A12}$$

The magnetic co-energy of the inductor in terms of tuning and harvesting circuits can be formulated as,

$$\delta WL = L_s \dot{q}_{32}^{(1)}(t)\delta \dot{q}_{32}^{(1)}(t). \tag{A13}$$

where the synthetic inductance value from Fig. 1b can be reduced from the equivalent impedance analysis, $Z_{in} = (Z_1 Z_3 Z_5)/(Z_2 Z_4)$ by allowing the relations $Z_1=R_1$, $Z_2=R_2$, $Z_3=R_3$, $Z_5=R_5$, and $Z_4= 1/(j\omega C_s)$ to give $Z_{in} = j\omega L_s$ [30, 32-33]. Therefore, the synthetic inductance value for tuning circuit can be formulated to give $L_s = (R_1 R_3 R_5 C_s)/R_2$, which is reduced in detail in Appendix B.

Appendix B. Synthetic inductance circuit for the shunt piezoelectric control

As given $L_s = (R_1 R_3 R_5 C_s)/R_2$ from Eq. (A13) and shown in Fig. 1, the Antoniou-type inductance circuit can simply be obtained using the configuration of the circuit terminal relations of the ideal op-amp systems connected with other circuit components. Under such condition, the two amplifiers with the differential gain $[G_1, G_2] \to \infty$ may result in $V_l(t) = V_a(t) = V_c(t)$ and $V_l(t) = V_c(t) = V_e(t)$ for the input terminals at nodes *a*, *c* and *e* (inverting and non-inverting terminals) and zero current flowing to these amplifiers. With the given input voltage $V_l(t) = L_s \frac{\mathrm{d}I_{32}^{(1)}(t)}{\mathrm{d}t}$ for the synthetic inductance, $\frac{V_l(s)}{I_{32}^{(1)}(s)} = sL_s$ can also be reduced using the Laplace transform where the parameter $I_{32}^{(1)}(s)$ can be calculated using the circuit analysis across the R_1, R_2, R_3, C_s, R_5 and the nodes *b* and *d*. Since zero current flows to the amplifiers, the current across R_5 or $I_{32}^{(1)}(s) = \frac{V_l(s)}{R_5}$ can be obtained first, and this may subsequently lead to the calculation of the capacitor voltage, giving the $V_{C_s}(s) = \frac{V_l(s)}{sC_s R_5}$ (note that capacitor current $I_{32}^{(1)}(t) = C_s \frac{\mathrm{d}V_{C_s}(t)}{\mathrm{d}t}$ or $V_{C_s}(s) = \frac{I_{32}^{(1)}(s)}{sC_s}$ in Laplace transform). The voltage between R_3 and C_s (voltage at node *d*) can be calculated to yield,

$$V_d(s) = V_{C_s}(s) + V_l = \frac{V_l(s)}{sC_s R_5} + V_l(s). \tag{B1}$$

As shown in Eq. (B1), the voltage and current across R_3 can be respectively formulated as,

$$V_{R_3}(s) = V_d(s) - V_l(s) = \frac{V_l(s)}{sC_s R_5}, \quad I_{R_3}(s) = \frac{V_{R_3}(s)}{R_3} = \frac{V_l(s)}{sC_s R_5 R_3}. \tag{B2}$$

Then the voltage across R_2 can easily be calculated using relation $I_{R_3}(s)$, giving,

$$V_{R_2}(s) = \frac{V_l(s) R_2}{sC_s R_5 R_3}. \tag{B3}$$

As shown in Eq. (B3), the voltage between R_1 and R_2 (voltage at node *b*) is given by,

$$V_b(s) = V_l(s) - V_{R_2}(s) = V_l(s) - \frac{V_l(s) R_2}{sC_s R_5 R_3}. \tag{B4}$$

Next, the voltage and current across R_1 gives respectively as,

$$V_{R_1}(s)=V_l(s)-\left(V_l(s)-\frac{V_l(s)R_2}{sC_sR_5R_3}\right) \text{ and } I_{R_1}(s)=\frac{V_l(s)-\left(V_l(s)-\frac{V_l(s)R_2}{sC_sR_5R_3}\right)}{R_1}=\frac{V_l(s)R_2}{sC_sR_5R_3R_1}. \quad \text{(B5)}$$

It implies that $I_{32}^{(1)}(s)=I_{R_1}(s)$ can be used to determine the earlier given relation of the inductance, which can be written in the final form, $\frac{V_l(s)}{\frac{V_l(s)R_2}{sC_sR_5R_3R_1}}=sL_s$ or $\frac{C_sR_5R_3R_1}{R_2}=L_s$, as required. Note that the Antoniou-type inductance and the Riordan-type inductance show different circuit topologies, but have the same formula of synthetic inductance [31]-[33].

Appendix C. Eigenmode of the nonhomogeneous and discontinuous cantilever smart beam with proof mass offset

The matrix elements of the characteristic equations in Eq. (21) can be expressed as,

$a_{11}=1$, $a_{12}=0$, $a_{13}=0$, $a_{14}=0$, $a_{15}=0$, $a_{16}=0$, $a_{17}=0$, $a_{18}=1$,

$a_{21}=0$, $a_{22}=1$, $a_{23}=0$, $a_{24}=1$, $a_{25}=0$, $a_{26}=0$, $a_{27}=0$, $a_{28}=0$,

$a_{31}=\cos\mu L_1$, $a_{32}=\sin\mu L_1$, $a_{33}=\cosh\mu L_1$, $a_{34}=\sinh\mu L_1$, $a_{35}=-1$, $a_{36}=0$, $a_{37}=-1$, $a_{38}=0$,

$a_{41}=-\sin\mu L_1$, $a_{42}=\cos\mu L_1$, $a_{43}=\sinh\mu L_1$, $a_{44}=\cosh\mu L_1$, $a_{45}=0$, $a_{46}=-1$, $a_{47}=0$, $a_{48}=-1$,

$a_{51}=C_{t1}\mu^3\sin\mu L_1$, $a_{52}=-C_{t1}\mu^3\cos\mu L_1$, $a_{53}=C_{t1}\mu^3\sinh\mu L_1$, $a_{54}=C_{t1}\mu^3\cosh\mu L_1$,

$a_{55}=0$, $a_{56}=C_{t2}\beta^3$, $a_{57}=0$, $a_{58}=-C_{t2}\beta^3$,

$a_{61}=-C_{t1}\mu^2\cos\mu L_1$, $a_{62}=-C_{t1}\mu^2\sin\mu L_1$, $a_{63}=C_{t1}\mu^2\cosh\mu L_1$, $a_{64}=C_{t1}\mu^2\sinh\mu L_1$,

$a_{65}=C_{t2}\beta^2$, $a_{66}=0$, $a_{67}=-C_{t2}\beta^2$, $a_{68}=0$,

$a_{71}=0$, $a_{72}=0$, $a_{73}=0$, $a_{74}=0$, $a_{75}=I_2^{tip}\omega^2\beta\sin\beta L_2-x_cI_0^{tip}\omega^2\cos\beta L_2-C_{t2}\beta^2\cos\beta L_2$,

$a_{76}=-I_2^{tip}\omega^2\beta\cos\beta L_2-x_cI_0^{tip}\omega^2\sin\beta L_2-C_{t2}\beta^2\sin\beta L_2$,

$a_{77}=-I_2^{tip}\omega^2\beta\sinh\beta L_2-x_cI_0^{tip}\omega^2\cosh\beta L_2+C_{t2}\beta^2\cosh\beta L_2$,

$a_{78}=-I_2^{tip}\omega^2\beta\cosh\beta L_2-x_cI_0^{tip}\omega^2\sinh\beta L_2+C_{t2}\beta^2\sinh\beta L_2$,

$a_{81}=0$, $a_{82}=0$, $a_{83}=0$, $a_{84}=0$, $a_{85}=-x_cI_0^{tip}\omega^2\beta\sin\beta L_2+I_0^{tip}\omega^2\cos\beta L_2+C_{t2}\beta^3\sin\beta L_2$,

$a_{86}=x_cI_0^{tip}\omega^2\beta\cos\beta L_2+I_0^{tip}\omega^2\sin\beta L_2-C_{t2}\beta^3\cos\beta L_2$,

$a_{87}=x_cI_0^{tip}\omega^2\beta\sinh\beta L_2+I_0^{tip}\omega^2\cosh\beta L_2+C_{t2}\beta^3\sinh\beta L_2$,

$a_{88}=x_cI_0^{tip}\omega^2\beta\cosh\beta L_2+I_0^{tip}\omega^2\sinh\beta L_2+C_{t2}\beta^3\cosh\beta L_2$.

To reformulate and simplify both mode shapes from Eq. (20), the unknown constants must be algebraically solved to give only one similar constant for both mode shapes. This equal constant can be presumed to be unity because the orthonormalisation-based Ritz method and its Ritz constants are utilised, such that the Ritz eigenfunction shows the accurate mode shapes. There are several forms to obtain the unknown constants from Eq. (21). Here, after manipulation and simplification, one example of the modified mode shapes with only remaining one similar constant A_1 can be formulated as,

$$W_k(x)=\begin{cases}W_{k1}(x)=A_1(\cos\mu x-\cosh\mu x)+B_1(\sin\mu x-\sinh\mu x), & 0\le x\le L_1\\ W_{k2}(x)=A_2\cos\beta x+B_2\sin\beta x+C_2\cosh\beta x+D_2\sinh\beta x, & 0\le x\le L_2\end{cases}, \quad \text{(C1)}$$

where $B_1 = -A_1 \dfrac{\lambda_N}{\lambda_D}$,

$$\lambda_N = a_{41} - a_{43} + \frac{a_{46}\left(\dfrac{-a_{75}a_{87}}{a_{85}} - a_{77}\right)\left(a_{61} - a_{63} - \dfrac{a_{65}\left(a_{31} - a_{33}\right)}{a_{35}}\right)}{\left(\dfrac{-a_{75}}{a_{85}} + a_{76}\right)\left(-a_{65} - \dfrac{a_{65}a_{37}}{a_{35}}\right)} + a_{46}\left(\frac{\left(\dfrac{-a_{75}a_{88}}{a_{85}} + a_{78}\right)}{\left(\dfrac{-a_{75}}{a_{85}} + a_{76}\right)} - a_{48}\right)\frac{\left(a_{51} - a_{53} + \dfrac{a_{56}\left(a_{41} - a_{43}\right)}{a_{46}}\right)}{\left(-a_{56} - \dfrac{a_{56}a_{48}}{a_{46}}\right)},$$

$$\lambda_D = a_{42} - a_{44} + \frac{a_{46}\left(\dfrac{-a_{75}a_{87}}{a_{85}} + a_{77}\right)\left(a_{62} - a_{64} - \dfrac{a_{65}\left(a_{32} - a_{34}\right)}{a_{35}}\right)}{\left(-\dfrac{a_{75}}{a_{85}} + a_{76}\right)\left(-a_{65} - \dfrac{a_{65}a_{37}}{a_{35}}\right)} + a_{46}\left(\frac{\left(\dfrac{-a_{75}a_{88}}{a_{85}} + a_{78}\right)}{\left(\dfrac{-a_{75}}{a_{85}} + a_{76}\right)} - a_{48}\right)\frac{\left(a_{52} - a_{54} - \dfrac{\left(a_{42} - a_{44}\right)a_{56}}{a_{46}}\right)}{\left(-a_{56} - \dfrac{a_{56}a_{48}}{a_{46}}\right)},$$

$$C_2 = -\frac{A_1\left(a_{61} - a_{63} - \dfrac{a_{65}\left(a_{31} - a_{33}\right)}{a_{35}}\right) + B_1\left(a_{62} - a_{64} - \dfrac{a_{65}\left(a_{32} - a_{34}\right)}{a_{35}}\right)}{\left(-a_{65} - \dfrac{a_{65}a_{37}}{a_{35}}\right)},$$

$$D_2 = -\frac{A_1\left(a_{51} - a_{53} - \dfrac{a_{56}\left(a_{41} - a_{43}\right)}{a_{46}}\right) + B_1\left(a_{52} - a_{54} - \dfrac{a_{56}\left(a_{42} - a_{44}\right)}{a_{46}}\right)}{\left(-a_{56} - \dfrac{a_{56}a_{48}}{a_{46}}\right)},$$

$$A_2 = -\frac{A_1\left(a_{31} - a_{33}\right) + B_1\left(a_{32} - a_{34}\right) + C_2 a_{37}}{a_{35}},\ B_2 = -\frac{A_1\left(a_{41} - a_{43}\right) + B_1\left(a_{42} - a_{44}\right) + D_2 a_{48}}{a_{46}}.$$

Eq. (C1) is essential formula for calculating the normalised eigenfunction in Eq. (14). Each part of Eq. (14) consists of the iterative normalised mode shape for each segment having the multiplication with the Heaviside functions for $H_1(x)=H(x)-H(x-L_1)$ and $H_2(x)=H(x)-H(x-L_2)$. It represents the eigenmode of the discontinuous structures with different mode shapes along the x-axis. At this point, whatever the chosen value x for satisfying $W_k(x)$ exists at the interval of the first segment $0 \le x \le L_1$, the mode shape with the unit step function of $H_1(x)$ turns to be active whereas the second segment with $H_2(x)$ for $0 \le x \le L_2$ is deactivated or zero, and vice versa.

References

[1] Reddy JN. On laminate composite plates with integrated sensors and actuators. Eng Struct 1997;21: 568– 93.

[2] Lam KY, Peng XQ, Liu GR, Reddy JN. A finite element model for piezoelectric composite laminates. Smart Mater Struct 1997; 6: 583–91.

[3] Moita JMS, Soares CMM, Soares CAM. Active control of forced vibrations in adaptive structures using a higher order model. Compos Struct 2005; 71: 349–55.

[4] Moita JMS, Correia IFP, Soares CMM. Active control of adaptive laminated structures with bounded piezoelectric sensors and actuators. Comput Struct 2004; 82(17–19): 1349–58.

[5] Krommer M, On the correction of the Bernoulli-Euler beam theory for smart piezoelectric beams. Smart Mater Struct 2001;10: 668–680.

[6] Krommer M, Irschik H. An electromechanically coupled theory for piezoelastic beams taking into account the charge equation of electrostatics. Acta Mech 2002; 154: 141–158.

[7] Deü JF, Benjeddou A. Free-vibration analysis of laminated plates with embedded shear-mode piezoceramic layers. Int J Solids Struct 2005; 42: 2059–2088.

[8] Schoeftner J, Buchberger G, Irschik H. Static and dynamic shape control of slender beams by piezoelectric actuation and resistive electrodes. Compos Struct 2014; 111: 66-74

[9] Gohari S, Sharifi S, Vrcelj Z. A novel explicit solution for twisting control of smart laminated cantilever composite plates/beams using inclined piezoelectric actuators. Compos Struct 2017; 161: 477-504.
[10] Irschik H, Krommer M, Pichler U. Dynamic shape control of beam-type structures by piezoelectric actuation and sensing. Int J Appl Electromagn Mech 2003; 17: 251–58.
[11] Schoeftner J. Bending moment tracking and the reduction of the axial stress in vibrating beams by piezoelectric actuation. Acta Mech 2017; 228: 3827–38.
[12] Gaudenzi P, Carbonaro R, Benzi E. Control of beam vibrations by means of piezoelectric devices: theory and experiments. Compos Struct 2000; 50: 373–9.
[13] Tzou HS, Tseng CI. Distributed vibration control and identification of coupled elastic/piezoelectric systems:finite element formulation and applications. Mech Syst Signal Process. 1991; 5: 215–31.
[14] Kapuria S, Yasin MY. Active vibration control of smart plates using directional actuation and sensing capability of piezoelectric composites. Acta Mech 2013; 224: 1185–99.
[15] Giorgio I, Culla A, Del Vescovo D. Multimode vibration control using several piezoelectric transducers shunted with a multiterminal network. Arch Appl Mech 2009; 79: 859–79.
[16] dell'Isola F, Maurini C, Porfiri M. Passive damping of beam vibrations through distributed electric networks and piezoelectric transducers: prototype design and experimental validation. Smart Mater Struct 2004; 13: 299–308.
[17] Maurini C, dell'Isola F, Del Vescovo D. Comparison of piezoelectronic networks acting as distributed vibration absorbers. Mech Syst Signal Proc 2004; 18:1243–1271.
[18] Preumont A 1997 Vibration Control of Active Structures (Dordrecht: Kluwer)
[19] Marakakis k, Tairidis GK, Koutsianitis P, Stavroulakis GE. Shunt piezoelectric systems for noise and vibration control: a review. Front Built Environ 2019; 5:64 doi: 10.3389/fbuil.2019.00064
[20] Forward RL. Electronic damping of vibrations in optical structures. Appl Opt 1979; 18: 690–7.
[21] Hagood NW, Chung WH, Flotow AV. Modelling of piezoelectric actuator dynamics for active structural control. J Intell Mater Syst Struct 1990; 1: 327–54.
[22] Caruso G. A critical analysis of electric shunt circuits employed in piezoelectric passive vibration damping. Smart Mater Struct 2001;10: 1059–68.
[23] Thomas O, Ducarne J, Deu JF. Performance of piezoelectric shunts for vibration reduction. Smart Mater Struct 2012; 21: 015008
[24] Vasques CMA. Improved passive shunt vibration control of smart piezo-elastic beams using modal piezoelectric transducers with shaped electrodes. Smart Mater Struct 2012; 21: 125003.
[25] Lefeuvre E, Badel A, Petit L, Richard C, Guyomar D. Semi-passive piezoelectric structural damping by synchronized switching on voltage sources. J Intell Mater Syst Struct 2006; 17: 653–660.
[26] Ducarne J, Thomas O, Deu JF. Structural vibration reduction by switch shunting of piezoelectric elements: modeling and optimization. J Intell Mater Syst Struct. 2010; 21: 797–816.
[27] Hollkamp JJ. Multimode passive vibration suppression with piezoeleciric materials and resonant shunts. J Intell Mater Syst Struct 1994; 5: 45–57.
[28] Fleming AJ, Behrens S, Moheimani SOR. Optimization and implementation of multi-mode piezoelectric shunt damping systems. IEEE/ASME Trans Mechatronics 2002; 7: 87–94.
[29] Moheimani SOR. Multimode piezoelectric shunt damping with a highly resonant impedance. IEEE Trans Control Syst Technol 2004; 12: 484–91.
[30] Antoniou A. Realisation of gyrators using operational amplifiers, and their use in RC-active-network synthesis. Proc Inst Electr Eng 1969; 116: 1838–50.
[31] Riodan RHS. Simulated inductors using differential amplifiers, Electr. Letters 1967; 3: 50–51.
[32] Sedra AS, Smith KC. Microelectronic Circuits. 7th Edition; New York: Oxford University Press; 2015.
[33] Dimopoulos HG. Analog Electronic Filters: Theory, Design and Synthesis. Springer Netherlands; 2012.
[34] Guyomar D, Badel A, Lefeuvre E, Richard C. Toward energy harvesting using active materials and conversion improvement by nonlinear processing. IEEE Trans Ultrason Ferroelectr Freq Control 2005; 52: 584–95.
[35] Lefeuvre E, Badel A, Richard C, Petit L, Guyomar D. A comparison between several vibration-powered piezoelectric generators for standalone systems. Sens Actuat A–Phys 2006;126: 405–16.
[36] Shu YC, Lien IC. Analysis of power output for piezoelectric energy harvesting systems. Smart Mater Struct 2006; 15: 1499-1512.

[37] Shu YC, Lien IC, Wu WJ. An improved analysis of the SSHI interface in piezoelectric energy harvesting. Smart Mater Struct 2007; 16: 2253–64.
[38] Goldschmidtboeing F, Woias P. Characterization of different beam shapes for piezoelectric energy harvesting. J Micromech Microeng 2008; 18: 104013.
[39] duToit, N.E., Wardle, B.L., Kim, S.-G.: Design considerations for MEMS-scale piezoelectric mechanical vibration energy harvesters. Int. J. Integrated Ferroelectrics. 71, 121–160 (2005).
[40] Dalzell P, Bonello P. Analysis of an energy harvesting piezoelectric beam with energy storage circuit. Smart Mater Struct. 2012; 21: 105029.
[41] Lumentut MF, Howard IM. Analytical and experimental comparisons of electromechanical vibration response of a piezoelectric bimorph beam for power harvesting. Mech Syst Signal Process 2013; 36: 66–86.
[42] Adhikari S, Friswell MI, Inman DJ. Piezoelectric energy harvesting from broadband random vibrations. Smart Mater Struct 2009; 18:115005.
[43] Ali SF, Friswell MI, Adhikari S. Piezoelectric energy harvesting with parametric uncertainty. Smart Mater Struct 2010; 105010.
[44] Wickenheiser AM. Eigensolution of piezoelectric energy harvesters with geometric discontinuities: Analytical modelling and validation. J Intell Mater Syst Struct 2013; 24: 729–44.
[45] Tang L, Wang J. Modeling and analysis of cantilever piezoelectric energy harvester with a new-type dynamic magnifier. Acta Mech 2018; 229: 4643–64.
[46] Faroughi S, Rojas EF, Abdelkefi A, Park, YH, Reduced-order modeling and usefulness of non-uniform beams for flexoelectric energy harvesting applications. Acta Mech 2019; 230: 2339–61.
[47] Lumentut MF, Howard IM. Parametric design-based modal damped vibrational piezoelectric energy harvesters with arbitrary proof mass offset: numerical and analytical validations. Mech Syst Signal Process 2016; 68: 562–86.
[48] Wang KF, Wang BL. An analytical model for nanoscale unimorph piezoelectric energy harvesters with flexoelectric effect. Compos Struct 2016. 153, 253-61.
[49] Lumentut MF, Howard IM. Intrinsic electromechanical dynamic equations for piezoelectric power harvesters. Acta Mech 2017; 228: 631–50.
[50] Friswell MI, Adhikari S. Sensor shape design for piezoelectric cantilever beams to harvest vibration energy. J App Phys 2010; 108: 014901.
[51] Lumentut MF, Howard IM. Electromechanical finite element modelling for dynamic analysis of a cantilevered piezoelectric energy harvester with tip mass offset under base excitations. Smart Mater Struct 2014; 23: 095037.
[52] Lumentut MF, Friswell MI. A smart pipe energy harvester excited by fluid flow and base excitation. Acta Mech 2018; 229: 4431–4458.
[53] Lu Q, Liu L, Scarpa F, Leng J, Liu Y. A novel composite multi-layer piezoelectric energy harvester. Compos Struct 2018; 201: 121–30.
[54] Lumentut MF, Francis LA, Howard IM. Analytical techniques for broadband multielectromechanical piezoelectric bimorph beams with multifrequency power harvesting. IEEE Trans Ultrason Ferroelectr Freq Control 2012; 59: 1555-68.
[55] Wang KF, Wang BL, Zeng S. Analysis of an array of flexoelectric layered nanobeams for vibration energy harvesting. Compos Struct, 2018; 187:48-57.
[56] Lin HC, Wu PH, Lien IC, Shu YC. Analysis of an array of piezoelectric energy harvesters connected in series. Smart Mater Struct 2013; 22: 094026.
[57] Wu PH, Shu YC. Finite element modeling of electrically rectified piezoelectric energy harvesters. Smart Mater Struct 2015; 24: 094008.
[58] Wu PH, Chen YJ, Li BY. Shu YC. Wideband energy harvesting based on mixed connection of piezoelectric oscillators. Smart Mater Struct 2017; 26: 094005.
[59] Lumentut MF, Howard IM. Effect of shunted piezoelectric control for tuning piezoelectric power harvesting system responses—analytical techniques. Smart Mater Struct 2015; 24: 105029.
[60] Lumentut MF, Howard IM. Electromechanical analysis of an adaptive piezoelectric energy harvester controlled by two segmented electrodes with shunt circuit networks. Acta Mech 2017; 228: 1321–1341.
[61] Lumentut MF, Shu YC. A unified electromechanical finite element dynamic analysis of multiple segmented smart plate energy harvesters: circuit connection patterns. Acta Mech 2018; 229: 4575-4604.

[62] Smits JG, Choi WS. The constituent equations of piezoelectric heterogeneous bimorphs. IEEE Trans Ultrason Ferroelectr Freq Contr 1991; 46: 256–269.
[63] Smits JG, Dalke SI, Cooney TK. The constituent equations of piezoelectric bimorphs. Sens Actuat A–Phys 1991; 28: 41–61.
[64] Lumentut MF, Howard IM. Analytical modeling of self-powered electromechanical piezoelectric bimorph beams with multidirectional excitation. Int J Smart Nano Mat 2011; 2: 134-175.
[65] Ritz W. Über eine neue Methode zur Lösung gewisser Variationsprobleme der mathematischen Physik. J. Reine Angew Math 1909; 135: 1–61.
[66] Courant R, Hilbert D. Methoden der mathematischen Physik /English Ed.: Methods of Mathematical Physics. New York; Interscience Publishers; 1953–1962.
[67] Mikhlin SG. Variational Methods in Mathematical Physics, New York, NY, USA; Pergamon Press: 1964.
[68] Ikeda T. Fundamentals of Piezoelectricity. New York: Oxford University Press; 1990.
[69] Tichý J, Erhart J, Kittinger E, Prívratská J. Fundamentals of Piezoelectric Sensorics. Berlin, Heidelberg: Springer; 2010.